Final Technical Report for USGS Awards G12AP20064 and G12AP20065

Expected Peak Ground Motions in the San Jacinto Valley from Dynamic Rupture Models with Constraints from Precariously Balanced Rocks: Collaborative Research between UC Riverside and SDSU

4/1/2012 – 3/31/2014

Principal Investigators*

Kim B. Olsen,
Dept of Geological Sciences, San Diego State University
5500 Campanile Dr., San Diego, CA 92182-2010
ph 619 594 2649
email kbolsen@mail.sdsu.edu

David Oglesby
Dept Earth Sciences, UC Riverside
900 University Ave, Riverside, CA 92521
ph 951 827 2036
email david.oglesby@ucr.edu

* J. Lozos, R. Takedatsu, J. Brune, and R. Brune contributed significantly to the work reported here.

Abstract

Southern California's San Jacinto Fault is geometrically complex, consisting of several major strands with smaller scale complexity within each strand. The two northernmost strands, the Claremont and the Casa Loma-Clark, are separated by a 25-km-long extensional stepover with an average of 4 km separation between the strands. We use a combined modeling method to assess probable rupture and ground motion behaviors for this stepover. First, dynamic rupture modeling on geometrically complex fault strands embedded in a state-of-the-art 3D crustal velocity model is used to generate a series of scenario earthquakes. We then use the resulting near-fault low-frequency (<1 Hz) ground motion time histories to generate ensemble broadband synthetic seismograms with a hybrid approach. These synthetics are then validated against leading Ground Motion Prediction Equations (GMPEs), and compared with a distribution of precariously balanced rocks (PBRs) near the fault to constrain our results and assess shaking hazard for the region surrounding the fault. Our dynamic models produce sources between M5.4 and M6.9, with rupture limits imposed by sharp contrasts in fault stress, or by geometrical barriers. The main stepover serves as a primary barrier to rupture in our model, producing event sizes that are consistent with the historical behavior of the San Jacinto Fault. The largest broadband synthetics are consistent with GMPEs and the distribution of PBRs, none of which experience accelerations that produce toppling probabilities significantly higher than zero. Thus, while the PBRs do not rule out any of our model scenarios, they confirm that our models produce realistic rupture extents and shaking. Our model results are in contrast to current seismic hazard maps for this area, which reflect peak ground accelerations that likely would have toppled the PBRs.

Bibliography of all publications resulting from the work performed under the awards:

Lozos, J.C., D.D. Oglesby, J.N. Brune, and K.B. Olsen (2012). Small intermediate fault segments can either aid or hinder rupture propagation at stepovers, *Geophys. Res. Lett.* **39**, L18305, doi:10:1029/2012GL053005.

Lozos, J. C. (2013). Dynamic rupture and ground motion modeling on realistically complex strike-slip faults, PhD dissertation, University of California, Riverside.

Lozos, J. C., D. D. Oglesby, J. N. Brune, and K. B. Olsen (2014). Rupture propagation and ground motion of strike-slip stepovers with intermediate fault segments, Bulletin of the Seismological Society of America, in review.

Final Technical Report

Introduction

The San Jacinto Fault is a major right-lateral strike-slip component of the San Andreas fault system in inland southern California. It and the San Andreas Fault jointly accommodate up to 80% of the plate boundary strain in the region (Fialko, 2006; Blisniuk *et al.*, 2010). Its entire length, from its approach to the San Andreas Fault in Cajon Pass near San Bernardino, to its terminus in the Imperial Valley, is ~230 km (Figure 1). However, its structure is not continuous for that whole length; it consists of several long strands, separated by stepovers or splays, some of which have considerably smaller-scale geometrical complexity as well.

The instrumental record of ruptures on the San Jacinto Fault includes eight M6+ events since 1890. Only two of these – the ~M6.9 1918 event near Hemet (Salisbury *et al*., 2012) and the M6.5 1968 Borrego Mountain earthquake (Allen *et al.*, 1968) - had measured surface rupture. Isoseismals for these and other events suggest that they were confined to individual strands of the fault (Sanders and Kanamori, 1984; Toppozada *et al*., 2002). These records suggest that, despite the length of the fault and its high slip rate, some property of the fault is restricting its rupture behavior to moderate events. Analysis of measured surface rupture traces (Wesnousky, 2008), as well as dynamic rupture models of fault stepovers (e.g. Harris and Day, 1993; Aochi *et al.,* 2000; Oglesby, 2008; Lozos *et al.,* 2012) and branches (Kame *et al.,* 2003; Duan and Oglesby, 2007) suggest that geometrical complexities often serve as endpoints for ruptures. Given the multi-stranded geometry of the San Jacinto fault, this may be one explanation for the moderate size of its historic events.

The northernmost of the major geometrical discontinuities along the San Jacinto fault trace is the extensional stepover between the Claremont strand, which runs from Cajon Pass to the city of San Jacinto, and the Casa Loma-Clark strand, which runs from Moreno Valley to 20 km ENE of Borrego Springs (Figure 1). The two strands overlap for 25 km along strike. The separation between the strands through the stepover region ranges from 2.5 to 5 km. A smaller strand of ~2.5 km length, the Farm Road, is positioned at the northern end of the overlap, halfway between the Claremont and Casa Loma strands. The primary fault strands bound the San Jacinto Valley, a 2.3 km deep pull-apart sedimentary basin (Park *et al*., 1995). Two moderate historic events - a ~M6.5 in 1899 and a ~M6.9 in 1918 - are known to have occurred in the stepover region. However, the paleoseismic record for both the Claremont (Onderdonk *et al.,* 2013) and the Casa Loma-Clark (Rockwell *et al.,* 2014) indicates that significantly larger events, some with 3+ m of slip, have occurred on each strand multiple times in the past, some close enough together in time to have possibly been a single rupture.

This returns to the questions of how fault complexity affects rupture length, what conditions lead to a rupture propagating through complexities that have served as barriers

in the past, and whether a single event can rupture across the stepover between the Claremont and Casa Loma-Clark strands of the San Jacinto fault. The average 4 km separation between the strands is the maximum extensional stepover width that allows jumping rupture in modeling studies of idealized disconnected stepovers (Harris and Day, 1993; Lozos *et al*., 2012), a result which bears out in analysis of historical rupture traces (Wesnousky, 2008). The presence of several dozen precariously balanced rocks (PBRs, see Figure 2) near the stepover region (Brune, 1996; Brune, 2002; Brune *et al*., 2006), however, indicates that something is preventing the ground acceleration near the faults from reaching the level required to topple the rocks. Whether this is an effect of the dynamics of extensional stepovers resulting in lower ground motion (Brune, 2002; Lozos *et al*., 2013), or an indication that the stepover is a primary barrier to rupture cannot be determined from historical data alone.

To address these questions, we implement a multi-tiered modeling approach. We use 3D dynamic rupture modeling to investigate the effects of complex fault geometry, stress conditions, and surrounding geology on rupture propagation and slip. While this method best describes the physics of the source, it is very computationally intensive; the discretization used in these models is such that only low-frequency ground motions are well resolved. However, toppling probabilities for PBRs are affected by both low-frequency (LF) and high-frequency (HF) ground motions (Purvance *et al.*, 2008). We therefore combine the near-fault LF (<1 Hz) ground motions time histories generated by the dynamic models with HF scattering functions (Olsen and Takedatsu, 2014) to produce broadband seismograms for each model rupture, while also accounting for additional complexity in the medium surrounding the faults. We then conduct toppling tests for models of the PBRs in the study area, using these synthetic seismograms. Any models that produce ground motions that would topple many of the rocks can be ruled out as plausible scenarios, but scenarios that produce ground motions that are consistent with the distribution of rocks may also indicate what types of rupture behaviors have happened in the past, as well as what intensity of ground shaking may be expected in the vicinity of the Claremont-Casa Loma stepover in the future.

Methods

Source Modeling

We model our earthquake sources using the 3D finite element code FaultMod (Barall, 2009), incorporating a slip-weakening Coulomb friction criterion (Ida, 1972; Palmer and Rice, 1973; Andrews, 1976) and a fully elastic medium. Our critical slip weakening distance is 0.4 m, and our dynamic coefficient of friction is 0.2; the static frictional coefficient varies around 0.6, depending on the stress state, as described below. Our mesh is generated within FaultMod, with 100 m elements immediately adjacent to the fault and 400 m elements in the far field. We nucleate rupture at specified locations by raising the shear stress to 10% above the yield stress and forcing the rupture to propagate outward over a 3 km radius.

Our model region covers the northwestern end of the San Jacinto fault in Cajon Pass southeast to Anza, site of a known seismic gap, for an overall system length of 106.8 km. The fault geometry along strike is based on the USGS Quaternary Faults Database (USGS, 2010); the Claremont strand is 75.6 km long, the Casa Loma-Clark is 55 km, and the Farm Road is 2.4 km. The actual fault geometry downdip is poorly constrained. Thus, for simplicity, we use a vertical dip for all three strands, as in the Southern California Earthquake Center (SCEC) Community Fault Model (Plesch *et al.,* 2007), an interpretation that is consistent with geology (Kendrick and Morton, 2012) and seismicity literature (Lin *et al.,* 2007). Our fault mesh is shown in Figure 3. The fault trace is likely to be smoother at depth than at the surface, but we retain the surface variation at depth, thus making this model setup an end member for complex fault geometry.

We implement a regional stress field combined with stochastic asperities. Seismicity relocation shows a regional stress orientation of N7E for the northern San Jacinto Fault (Hardebeck and Hauksson, 2001). We use a N7E-oriented stress tensor that produces a stress drop of 5.5 MPa and a strength parameter S of 0.6 (defined as the difference between the yield stress and the initial shear stress, divided by the dynamic stress drop) when resolved onto a planar fault of the average strike of the San Jacinto Fault, as in Lozos' (2013) lower-resolution models of the Claremont-Casa Loma stepover. This low S value would result in supershear rupture velocities on a planar fault in a homogeneous setting, but the complexity of our model prevents the rupture front from exceeding the sheer wave velocity. We then resolve this homogeneous tensor onto our complex fault geometry, which results in a pattern of effective higher and lower stress drops that corresponds with the bends in the fault.

In order to account for additional stress complexity at a smaller scale than that of the geometrical variation, or is not directly generated by fault geometry, we also include stochastically-generated shear stress asperities, using the method of Andrews and Barall (2011), which creates a random self-similar shear stress distribution based on fault dimensions, a specified normal stress value, and four random number seeds. We use the average normal stress value from the regional stress field, and four sets of random numbers, to produce four different stochastic shear stress distributions. We then combine each resulting set of asperities with the regional stress field by subtracting the average shear stress value for the regional stress field from the shear stress value at each point of the stochastic stress field, then adding the remaining shear stress back to the regional value at that same point. Lastly, we taper the stresses toward the surface to a value of 10% of their value at depth over the top 3 km of the fault, and set the minimum shear stress value to 0 MPa in order to prevent the fault from slipping left-laterally. The resulting shear stress fields, prior to tapering, are shown in Figure 4. The lettered dots are forced nucleation locations, selected because they correspond with large areas of high shear stress.

We assign 3D material properties from the SCEC Community Velocity Model (CVM-S, Magistrale *et al.,* 2000) to the modeled volume. Contrasts in material properties can affect the dynamics of earthquake rupture (Harris and Day, 1997; Andrews and Ben Zion, 1997; Lozos *et al.,* 2013), so we include them even though the dynamic models are not used to determine ground motions at higher frequencies. We nevertheless clip the

minimum S-wave velocity to 1200 m/s, such that the dynamic models still resolve low-frequency ground motions up to an estimated 1 Hz.

Broadband Models

To include the HF component of the ground motions at the PBR sites, we use the hybrid broadband generation method BBtoolbox V1.5 (Olsen and Takedatsu, 2014). This method combines deterministic LF synthetics computed using kinematic or dynamic descriptions in 1D or 3D media, with HF scatterograms. The HF scatterograms are generated for each component of motion based on the theory for multiple S-to-S scattering by Zeng et al. (1991, 1993). The scatterograms are based on user-specified site-scattering parameters and are partly based on the site-specific velocity structure. The seismic scattering wave energy is realized to appear after the direct P wave arrival time, which is found from 3D ray tracing (Hole, 1992). Finally, the scatterograms are convolved with an appropriate source-time function. It is assumed that the scattering operators and moment release originate throughout the fault, but starts at the hypocenter. The hybrid broadband seismograms are calculated in the frequency domain using a simultaneous amplitude and phase matching algorithm (Mai and Beroza, 2003).

The version of BBtoolbox used here (V1.5, Olsen and Takedatsu, 2014) has been revised from previous versions (Mai *et al.,* 2010; Mena *et al.,* 2010) in several ways, as part of the SCEC Broadband validation exercise Phase 1 (Goulet *et al.,* 2014). The major revisions include "anchoring" the HF component to a theoretical level rather than the LF at the merging frequency, and a different source time function convolved onto the HF scatterograms. BBtoolbox V1.5 was one of three methods that passed the SCEC validation exercise, based on comparison of PSAs from synthetic to recorded broadband ground motions for more than 10 historical events (M_w4.6-7.2) as well as to Ground Motion Prediction Equations (GMPEs) (M_w5.5-6.6 events).

As described above, the LFs are generated by dynamic rupture models, using a CVM with an artificial cut-off of V_s^{min}=1200 m/s. However, near-surface S-wave velocities are typically somewhat lower than this cut-off value at the precarious rock sites, and for this reason we apply frequency-dependent amplification functions (Campbell and Bozorgnia, 2008) as a post-processing step. These amplification functions depend on the ratio between the actual V_{s30} and that used in the simulations (the reference V_s). However, the SCEC CVM-S surface velocities for rock sites tend to be biased high, and the spatial resolution near rock sites surrounded by sediments is limited. For these reasons, we set the V_{s30} for all PBR sites to be 760 m/s, in agreement with average near-surface V_s values found in connection with PBR site investigations (Pullammanappallil et al., 2008; Louie et al., 2010).

PBR Data and Methods

The precariously balanced rocks considered in this study are indicated by the red triangles in Figure 2. Some of these sites have been used in previous studies to assess

shaking intensities of historic and recent paleoseismic earthquakes in inland Southern California (Brune, 2002; Brune *et al.,* 2006), as well as in comparison with probabilistic seismic hazard estimates (Purvance *et al.,* 2008). Many of them, however, have been described more recently, with the specific purpose of assessing ground motions near the Claremont-Casa Loma stepover. Nearly all of the PBRs in this study are the fairly uniform granite of the Perris block, which crops out in low bouldery hills that are characteristic of the region. The exceptions are GV01, GV05, and SW01, which are composed of San Bernardino Mountains granite.

The process of evaluating a PBR for sensitivity to ground motion begins by making a 3D model of the surface of the rock, from XYZ Cartesian coordinates. For the purpose of this study, this task is accomplished by covering the rock and pedestal with photogrammetric targets, taking photographs from many angles, and processing them into a 3D model with the commercial software Photomodeler.

Photomodeler represents the surface of the rock by connecting the coordinate points of the targets to make abutting scalene triangles. The center of each triangle is considered to be the triangle's center of mass, and the area of each triangle corresponds to the triangle's mass relative to the whole rock. The collective center of mass of all the triangles of is calculated and plotted in XYZ coordinates, then added into the 3D model of the rock. This produced an XYZ coordinate point representing the center of mass of the rock. The azimuth that the rock would most easily topple toward is then determined, and the toppling angle for that azimuth is calculated. Two toppling angles are assigned: a_1 is the direction in which the rock most easily topples, and a_2 is the angle required to topple the rock when force is applied from an azimuth of 180 degrees from a_1.

We use this method to model 19 of the 20 PBRs considered in this study; the exception is rock SJ06, which is described by a rougher generic approximation (photomodeler representation currently unavailable). Location, size, and shape parameters for each rock are listed in Table 1. We then use the method of Purvance et al. (2008) to develop a fragility plot for each rock over a range of peak ground acceleration (PGA) and PGA-normalized spectral accelerations at 1 second (SA-1s). Figure 5 shows example fragility curves for several of the PBR sites.

In order to determine PGA and SA-1s from our model ruptures, we only consider the N-S and E-W components of the synthetic seismograms. We then plot these values for each event onto the fragility curve for each rock, to find the toppling probability in that event. Because we are using actual waveforms for these calculations, we do not have to assume that the maximum hazard values for PGA and SA-1s are generated by the same event; this also allows us to assess which rocks are more sensitive to which of the two parameters. Fragility curves become less precise as probabilities of toppling go to zero; we do not provide exact values for these lowest probabilities due to this loss of precision, and describe them as near-zero instead.

Results

Dynamic Models

Of the sixteen source models we conducted, only two (scenarios A1 and A2) produce jumping rupture across the stepover, from the Claremont onto the Casa Loma. In both of these cases, the end of the Claremont overlaps a high stress asperity on the Casa Loma; even then, the rupture does not produce significant slip on the Casa Loma before dying out. The larger of these two scenarios, A1, has a moment magnitude of 6.9. Three of the other model events (B2, C1, and D2) are also M6.9s, though these ruptures only involve the Claremont strand. Slip distributions for the four largest events are shown in Figure 6. The smallest event modeled is a M5.4; the majority of the model ruptures are in the range of M6.2 to M6.5. These magnitudes are consistent with historical events on the San Jacinto Fault, though their average slip is closer to 1 m, as opposed to the average 3 m of slip seen in some paleoseismic events (Rockwell *et al.,* 2014; Onderdonk *et al.,* 2014). Slip plots for these models are included in Appendix A. Models with the forced nucleation point on the Casa Loma strand consistently produce shorter ruptures with less slip, and therefore smaller moment, than ruptures with the forced nucleation point on the Claremont strand.

In all cases, rupture remains confined to the high shear stress asperities created by combining the regional and stochastic stress fields, with the largest amounts of slip corresponding to the regions of highest initial shear stress. Due to the pattern of these asperities, the majority of the ruptures do not even approach the stepover region itself, and thus do not address the issue of the overall ability of rupture to jump. However, the Lozos (2013) study of this stepover, using a larger grid size, included similar models using only the regional stress field. These also did not allow the rupture front to reach the stepover region in most cases, suggesting that features of the fault geometry and assumed regional stress field, independent of any random stress distribution, still discourage jumping rupture.

We chose to take only the four largest dynamic source models (shown in Figure 6) through to broadband ground motion modeling. Even though smaller events do not necessarily have weaker shaking than larger ones at high frequencies (affecting PGA), they do at lower frequencies (affecting SA-1s) that are still critical to toppling PBRs. However, this shaking affects a smaller area. The larger events have the potential to affect more of the PBRs, which makes them better points of comparison against these data.

Broadband Results

Figure 2 shows the location of 20 PBR sites (listed in Table 1) in the vicinity of the three faults involved in the dynamic rupture modeling in our study (Claremont, Farm Road, and Casa Loma). We generated three-component broadband seismograms at all stations for the four selected rupture scenarios including frequency-dependent site

amplification corrections using the method of Olsen and Takedatsu (2014, see Appendix B, Figs. B.1-4 for the synthetic accelerograms). The accelerograms are characterized by 10-15 s duration of strong shaking, as expected from M_w~6.9 events (e.g., the M6.9 1989 Loma Prieta, California earthquake, see for example, Chin and Aki, 1991). In order to capture the variability from the stochastic component of the scatterograms, we calculated ensemble average peak ground accelerations (PGAs), peak ground velocities (PGVs) and spectral accelerations at periods of 1s (SA-1s) from the synthetic ground motions (Tables 2-4). The largest horizontal PGAs (>0.5g) occur at the PBRs SJ05 (0.76g), SJ04 (0.67g), SJ02 (0.57g), LPN (0.57g) and PVLM (0.57g) for scenario C1, and UCR (0.53g) for scenario D2. Horizontal PGVs above 0.4 m/s occur at LPN (0.43 m/s) and SJ06 (0.42 m/s) for scenario B2; at SJ04 (0.45 m/s) and SJ05 (0.41 m/s) for scenario C1; and at UCR (0.40 m/s) for scenario D2. Finally, SA-1s values exceeding 0.3g are found for at SJ02 (0.30g) for scenario B2, at PVML (0.33g), SJ05 (0.38g), LPN (0.33g), SJ02 (0.34g), SJ04 (0.37g) and SJ05 (0.38g) for scenario C1, and at UCR (0.33g) for scenario D2.

Figure B.5 (Appendix) shows a comparison between our ensemble PGAs and SA-1s from our broadband synthetics against leading Ground Motion Prediction Equations (GMPEs, Abrahamson and Silva, 2008; Boore and Atkinson, 2008; Campbell and Bozorgnia, 2008) using the rotD50 metric (Boore et al., 2006). In general, the ground motion intensities from our BBs fall within one standard deviation of the median values, and are therefore considered in agreement with the GMPE predictions. The GMPE values were obtained for Vs30=760 m/s, the values used for the site corrections applied to the BBs.

It is clear from the broadband ground motions that the cluster of PBRs including SJ02 and SJ04-08 consistently account for some of the largest ground motions due to the close proximity to the Claremont strand (~4km) and therefore are critical to the toppling analysis. Moreover, rupture directivity is likely an important factor in controlling the peak ground motions, as revealed by the generally larger than median GMPE values of PGA, PGV, and SA-1s toward the southeastern end of the Claremont strand in scenario C1 (e.g, SJ02, SJ04-8), in which rupture nucleated at the northwestern end of the Claremont and propagated south-eastward. On the other hand, peak motions at SW01, GV01, and GV05, located near the initiation of rupture and mostly in the backward rupture direction for scenario C1, experienced lower than the median GMPE ground motion intensities.

PBR Results

Essentially all of the waveforms at all of the PBR sites have a near-zero or very low probability of toppling the rocks. Nonzero probabilities are found at site SJ06 (5%) for scenario A1, and at SJ08 and SJ05 (5%) for scenario C1. However, because our fragility calculations are based on extrapolations from synthetic seismograms, rather than from PSHAs, any toppling probability of 20% or lower is questionably different from zero. Thus, the distribution of precarious rocks is consistent with the ground motions from these model earthquakes.

Discussion

The complexity of our San Jacinto Fault parameterization is such that our models produce events of a size consistent with the historic record. As mentioned above, rupture propagation remains confined to high-stress asperities, the shape of which is defined by the combination of the regional stress field with stochastic stresses. Because the pre-stress field in our models is a combination of several types of complexity, however, it is difficult to say which factor may be dominant on the real-world San Jacinto Fault. However, given that the fault geometry is fixed, the geometrical component of the stress complexity alone cannot be responsible for controlling whether a rupture falls in the ~M6-7 range of the San Jacinto Fault's historic behavior, or whether it has the average of ~3 m slip as seen in the paleoseismic record (Onderdonk et al., 2013; Rockwell et al., 2014).

The result that the Claremont strand consistently has larger events than the Casa Loma strand is a combined effect of geometry and stress orientation. The Claremont strand is more planar than the Casa Loma in this interpretation of the fault geometry. It is also more favorably aligned within the current regional stress field (see Lozos (2013) for more discussion of this effect). But, as mentioned previously, the paleoseismic record for both strands includes events with an average of 3 m of slip. A smoother fault geometry at depth would likely permit longer ruptures on both strands, as the regional stress field would resolve more smoothly onto the trace, leading to asperities, but this also suggests that stress changes induced by factors other than the fault geometry would be needed to promote an end-to-end rupture on the Casa Loma-Clark strand. Rotations of local and regional stresses have been observed and documented after other large earthquakes in southern California (Hauksson, 1994; Hardebeck and Hauksson, 2001), and rotations of 10° in either direction from N7E produced very different rupture patterns on this same fault geometry in lower-resolution models (Lozos, 2013). It is likely that the average fault stress field at the time of this large Casa Loma-Clark event was oriented differently from the current regional stress orientation of N7E.

Our maximum event sizes are at odds with the most recent Uniform California Earthquake Rupture Forecast (UCERF3, Field et al., 2013), which suggests that the San Jacinto Fault has a M7.4 to M8.3 rupture on average of every 200 years, and few events below M7. One reason for this extreme discrepancy between our models and UCERF3 may be the geometrical parameterization of the fault. UCERF3 uses a single fault with few bends to represent the Claremont and Casa Loma-Clark, omitting the primary rupture barrier of the stepover. Our models are an opposite end member; our projection of the complex Quaternary Faults Database geometry to the full seismogenic depth of the fault likely induces more barriers than actually exist. However, our model event sizes are consistent with the historic series of ~M6 to ~M7 ruptures on the San Jacinto Fault, while that range is underrepresented by UCERF3. The lower estimate of UCERF3's maximum San Jacinto event size, M7.4, is consistent with paleoseismic events with ~3 m of slip that we fail to reproduce with the stress parameters used in this study. However, magnitude-scaling calculations (Wells and Coppersmith, 1994) indicate that M8.3 would require a rupture of over 1000 km in length (given the seismogenic depth of 16 km in common between our models and UCERF3), which is substantially longer than the combined

length of the Claremont and Casa Loma-Clark strands. More slip or a higher stress drop would somewhat decrease this required length, but our low-frequency dynamic models (Lozos, 2013) show that, for a given rupture length, a higher stress drop produces stronger ground motions. These stronger motions, as well as the higher SA-1s that would be produced by a M8.3 rupture, would likely produce toppling probabilities for the PBRs that are well above zero.

The velocity structure proves to have the most controlling influence on the ground motion. Our lower-resolution dynamic models (Lozos, 2013) produce their strongest ground motions in sedimentary basins, most notably the San Bernardino Basin and, to a lesser degree, the San Jacinto Valley. Outside of the basins, the strongest shaking is confined within ~5 km of the fault. The lineament of precarious rocks between the San Jacinto and Elsinore Faults, as described by Brune *et al.,* (2006), is consistent with these results, as the majority of these rocks are over 10 km from either fault.

Rupture directivity has little effect on ground motion within a basin that is directly on the fault; however, ground motion distributions and intensities from parts of the fault that cut through harder rock are more affected by directivity and by velocity structure in the far field (Lozos, 2013). In our low-frequency models, northwestward-directed rupture on the Claremont strand, for example, is more likely to excite stronger ground motions toward the northwest, specifically in the San Bernardino Valley and Cajon Pass, while southward-directed rupture on the Claremont produces stronger shaking in the San Jacinto Valley and San Gorgonio Pass, even if rupture does not jump.

Precariously balanced rocks do not occur on sedimentary basins, as these formations cannot weather out of solid bedrock that is covered with several kilometers of sediment (Bell *et al.,* 1998). Thus, all of the PBRs in this study are on solid rock sites; the amplified ground motions in the basins within our model do not significantly affect the PBRs. All experience a near-zero probability of being toppled in any of our model events, despite many of them being within 5 km of the fault. Thus, the existence and position of these rocks is consistent with all of our models. This means we are not able to use the precarious rocks to rule out any of our model scenarios. However, the fact that the majority of the PBRs, including the cluster of sites SJ02 and SJ04-SJ08, are toward the southeastern end of the Claremont strand, very close to the stepover, while relatively few exist in Cajon Pass and the San Bernardino Mountains, may imply a preferential northwestward rupture direction on the Claremont.

The presence and specific distribution of the PBRs is not consistent with the accelerations given a 2% chance of exceedance in 50 years for the region around the northern San Jacinto Fault by the National Seismic Hazard Map (Petersen *et al.,* 2014). The 2008 version of this map (Petersen *et al.,* 2008) revises the value downward from the 2002 version (Frankel *et al*., 2002), but the 0.8 g given in the 2014 version of the map would not result in near-zero toppling probabilities for the rocks.

We are not able to elaborate on whether the persistence of the rocks closest to the stepover region is a result of weaker shaking between the faults within a single event. This is largely because neither of our models that produced jumping rupture involved sustained rupture on both the Claremont and Casa Loma-Clark strands, and because we

only calculated broadband ground motions for one of these two. However, the paleoseismology of the Claremont and Casa Loma-Clark strands includes several events on both strands that overlap in time, which could be interpreted as single ruptures that jumped the stepover (Rockwell *et al.,* 2014). If these did occur, they did not produce ground motions strong enough to topple the rocks, which is consistent with the idea of reduced ground motion within the stepover (Brune, 2006; Lozos *et al.,* 2013).

The precarious rocks and the model ruptures alike emphasize that the Claremont/Casa Loma-Clark stepover is a robust barrier to rupture, and that only rare events may slip both strands at once. Complexity of the fault trace, the stress field, and the velocity structure combine to result in short ruptures with subshear rupture velocity and a limited area of strong shaking, even with initial stress drop and fault strength values that would result in prolonged supershear rupture on a planar fault in a homogeneous setting. Because the asperities in our models were generated randomly, we cannot say that our models produced events that are completely analogous to past events or possible future ones. A better understanding of the location of the real asperities would be necessary to assess this. However, the general consistency of our models with the historic behavior of the San Jacinto implies that a great deal of heterogeneity is controlling that behavior. The precarious rock data emphasizes that our modeled ground motions, despite the random asperities, are consistent with the real world as well.

Conclusions

The historic rupture behavior of the San Jacinto Fault is characterized by moderate events constrained to a single strand of the fault. Our dynamic model results are consistent with this behavior, and imply that a combination of geometrical complexity and geometrically-independent stress complexity is what keeps rupture confined to relatively short fault lengths. Under the current regional stress orientation, the Claremont strand is more favorable for longer ruptures than the Casa Loma-Clark strand. Paleoseismic data imply larger events on the northern San Jacinto, possibly involving both strands; this observation suggests that non-geometrically-induced stress evolves over time, and sometimes allows larger events. Future modeling studies accounting for this evolution of stresses will be needed to assess what conditions are necessary to produce these longer ruptures.

All of our simulated broadband ground motions are consistent with the distribution of PBRs near the San Jacinto Fault; none of the rocks experience a toppling probability of significantly greater than zero in any of our scenario earthquakes. The PBRs do not allow us to rule out any of our scenarios, but they do emphasize that our model rupture behaviors are consistent with real behaviors.

The presence of PBRs also suggests that, even in the larger events that are inferred from paleoseismic data but do not occur in our models, strong ground motions are confined to basin areas and immediately adjacent to the fault (<~3 km). It is interesting to note both that the greatest concentration of PBRs in the model area is close to the stepover region, and that the majority of the PBRs that experience non-zero

toppling probabilities are within this cluster. The peak motions responsible for these non-zero (although consistent with the presence of the PBRs) toppling probabilites in our models, are typically affected by rupture directivity effects (e.g., the large peak motions at the SJ PBR cluster for scenario C1 initiating at the NW end of the Claremont strand). It is a reasonable assumption that this rupture configuration would be most likely to generate toppling probabilities in the range inconsistent with the PBRs for the rare, large events not captured by our limited sample of rupture models. Moreover, there are relatively few mapped PBRs to the northwestern end of the Claremont and southeastern end of the Casa Loma-Clark. These findings may imply preferred rupture directions of SE to NW on the Claremont strand and, to a lesser degree, NW to SE on the Casa Loma-Clark, in both cases away from the stepover.

Our ground motions results are consistent in general location and distribution with the National Seismic Hazard Map (Petersen *et al.,* 2014), but our intensities are substantially lower than the 2% in 50 years probabilities given on the map. Our rupture lengths are also inconsistent with the maximum event sizes for the San Jacinto that are predicted by UCERF3 (Field *et al.,* 2013). However, if the maximum event sizes from UCERF3 or the peak ground motions from the National Seismic Hazard Map had previously occurred, many of the precariously balanced rocks in our study area would have been toppled. Our results therefore suggest that UCERF's maximum event sizes for the San Jacinto Fault may be implausible, and that the National Seismic Hazard Map's ground motion estimates for western Riverside and San Bernardino counties locally skew high. We suggest that realistically complex dynamic rupture simulations may help constrain plausible behaviors for major faults in future probabilistic earthquake rupture forecasts, and that hybrid deterministic-stochastic broadband ground motion modeling of regions and faults currently identified as high-hazard may help refine and constrain values for future seismic hazard mapping.

References

Abrahamson, N. A., and W. J. Silva (2008). Summary of the Abrahamson & Silva NGA Ground-Motion Relations, *Earthquake Spectra*, 24(1), 67-97.

Allen, C. R., A. Grantz, J. N. Brune, M. M. Clark, R. V. Sharp, T. G. Theodore, E. W. Wolfe, and M. Wyss (1968). The Borrego Mountain, California, earthquake of 9 April 1968: a preliminary report, *Bulletin of the Seismological Society of America* **58**, 1183-1186.

Andrews, D. J. (1976). Rupture propagation with finite stress in antiplane strain, *Journal of Geophysical Research* **81,** 3575-3582.

Andrews, D. J., and Y. Ben-Zion (1997). Wrinkle-like slip pulse on a fault between different materials*, Journal of Geophysical Research* **102**, 553–571.

Andrews, D. J., and M. Barall (2011). Specifying initial stress for dynamic heterogeneous earthquake source models, *Bulletin of the Seismological Society of America* **101**, 2408-2417.

Aochi, H., E. Fukuyama, and M. Matsu'ura (2000). Spontaneous rupture propagation on a non-planar fault in 3-D elastic medium, *Pure and Applied Geophysics* **157**, 2003–2027.

Barall, M. (2009). A grid-doubling technique for calculating dynamic three-dimensional spontaneous rupture on an earthquake fault, *Geophysical Journal International* **178**, 845–859.

Bell, J. W., J. N. Brune, T. Liu, M. Zerda, and J. C. Yount (1998). Dating the precariously balanced rocks in seismically active parts of California and Nevada, *Geology* **26**, 495-498.

Blisniuk, K., T. Rockwell, L. Owen, M. Oskin, C. Lippincott, M. Caffee, and J. Dortch (2010). Late Quaternary slip rate gradient defined using high-resolution topography and 10Be dating of offset landforms on the southern San Jacinto fault zone, California, *Journal of Geophysical Research* **115**, 1–11, B08401.

Boore, D.M., and G.M. Atkinson (2008). Ground-motion prediction equations for the average horizontal component of PGA, PGV, and 5%-damped PSA at spectral periods between 0.01 and 10.0 s, *Earthquake Spectra* 24, No. 1, pages 99-138.

Brune, J. N. (1996). Precariously balanced rocks and ground motion maps for southern California, *Bulletin of the Seismological Society of America* **86**, 43-54.

Brune, J. N. (2002). Precarious-rock constraints on ground motion from historic and recent earthquakes in southern California, *Bulletin of the Seismological Society of America* **92**, 2602-2611.

Brune, J. N., A. Anooshehpoor, M. D. Purvance, and R. J. Brune (2006). Band of precariously balanced rocks between the Elsinore and San Jacinto, California, fault zones: constraints on ground motion for large earthquakes, *Geology* **34**, 137-140.

Campbell, K. W. and Y. Bozorgnia (2008). NGA ground motion model for the geometric mean horizontal component of PGA, PGV, PGD and 5% damped linear elastic response spectra for periods ranging from 0.01 to 10s, *Earthquake Spectra* **24(1)**, 139-171.

Chin, B-H., and K. Aki (1991). Simultaneous study of the source, path, and site effects on strong motion during the 1989 Loma Prieta earthquake: a preliminary on pervasive nonlinear site effects, *Bulletin of the Seismological Society of America* **81**, 1859-1884.

Duan, B., and D. D. Oglesby (2007). Nonuniform prestress from prior earthquakes and the effect on dynamics on branched fault systems, *Journal of Geophysical Research* **112**, B05308, doi:10.1029/2006JB004443.

Fialko, Y. (2006). Interseismic strain accumulation and the earthquake potential of the southern San Andreas fault system, *Nature* **441**, 968–971.

Field, E. H., G. P. Biasi, P. Bird, T. E. Dawson, K. R. Felzer, D. D. Jackson, K. M. Johnson, T. H. Jordan, C. Madden, A. J. Michael, K. R. Milner, M. T. Page, T. Parsons, P. M. Powers, B. E. Shaw, W. R. Thatcher, R. J. Weldon II, and Y. Zeng (2013). Uniform California earthquake rupture forecast, version 3 (UCERF3)—The time-independent model, *U.S. Geological Survey Open-File Report* 2013–116., *California Geological Survey Special Report* 228, and *Southern California Earthquake Center Publication* 1792.

Frankel, A. D., M. D. Petersen, C. S. Mueller, K. M. Haller, R. L. Wheeler, E. V. Leyendecker, R. L. Wesson, S. C. Harmsen, C. H. Cramer, D. M. Perkins, and K. S. Rukstales (2002), Documentation for the 2002 update of the National Seismic Hazard Maps, *U.S. Geological Survey Open File Report* 02-420.

Goulet, C.A., and N.A. Abrahamson (2014). The SCEC Broadband Platform validation exercise: methodology for code validation in the context of seismic hazard analyses, *Seismological Research Letters*, in review.

Hardebeck, J. L., and E. Hauksson (2001). Crustal stress field in southern California and its implications for fault mechanics, *Journal of Geophysical Research* **106**, 21859-21882.

Harris, R. A., and S. M. Day (1993). Dynamics of fault interaction: parallel strike-slip faults, *Journal of Geophysical Research* **98,** 4461-4472.

Harris, R. A., and S. M. Day (1997). Effects of a low-velocity zone on dynamic rupture, *Bulletin of the Seismological Society of America* **87**, 1267–1280.

Hauksson, E. (1994). State of stress from focal mechanisms before and after the 1992 Landers earthquake sequence, *Bulletin of the Seismological Society of America* **84**, 917-934.

Hole, J. A. (1992). Non-linear high resolution three-dimensional seism travel time tomography, *Journal of Geophysical Research* **97**, 6553-6562.

Ida, Y. (1972). Cohesive force across the tip of a longitudinal shear crack and Griffith's specific surface energy, *Journal of Geophysical Research* **77,** 3796-3805.

Kame, N., J. R. Rice, and R. Dmowska (2003). Effects of pre-stress state and rupture velocity on dynamic fault branching, *Journal of Geophysical Research* **108,** 2265, doi: 10.1029/2002JB002189.

Kendrick, K. J., and D. M. Morton (2012). "Geomorphic evidence for structural evolution of the northern San Jacinto fault zone in the San Timoteo badlands." Seismological Society of America Annual Meeting, Town and Country Resort and Convention Center, San Diego, California. Conference presentation.

Lin, G., P. M. Shearer, and E. Hauksson (2007). Applying a three-dimensional velocity model, waveform cross correlation, and cluster analysis to locate southern

California seismicity from 1981 to 2005, *Journal of Geophysical Research* **112**, doi: 10.1029/2007JB004986.

Lozos, J. C., D. D. Oglesby, J. N. Brune, and K. B. Olsen (2012). Small intermediate fault segments can either aid or hinder rupture propagation at stepovers, *Geophysical Research Letters* **39**, doi:10.1029/2012GL053005.

Lozos, J. C., D. D. Oglesby, and J. N. Brune (2013). The effects of fault stepovers on ground motion, *Bulletin of the Seismological Society of America* **103,** 1922-1934.

Lozos, J. C. (2013), Dynamic rupture and ground motion modeling on realistically complex strike-slip faults, *PhD dissertation, University of California, Riverside.*

Louie, J.N., J.N. Brune, and S.K. Pullammanappallil (2010). Estimates of Vs100 at sites of precariously balanced rocks. 2010 SCEC Annual Meeting September 2010 poster 1-073; http://www.scec.org/meetings/2010am/index.html (Revised p0ster abstract 1-073).

Magistrale, H., S. Day, R. Clayton, and R. Graves (2000). The SCEC southern California reference three-dimensional seismic velocity model version 2, *Bulletin Seismological Society of America* **90 (6B),** S65-S76.

Mai, P.M. and G.C Beroza (2003). A hybrid method for calculating near-source, broadband seismograms: Application to strong motion prediction, *Physics of the Earth and Planetary Interiors* **137**, no 1-4, 183-199.

Mai, P.M., W. Imperatori and K.B. Olsen (2010). Hybrid broadband ground-motion simulations: combining long-period deterministic synthetics with high-frequency multiple S-to-S backscattering, *Bulletin of the Seismological Society of America* **100**, 5A, 2124-2142, doi: 10.1785/0120080194.

Mena, B., P.M. Mai, K.B. Olsen, M.D. Purvance, and J.N. Brune (2010). Hybrid broadband ground-motion simulation using scattering Green's functions: application to large-magnitude events, *Bulletin of the Seismological Society of America* **100**, 5A, 213-2122, doi: 10.1785/0120080318.

Oglesby, D. D. (2008). Rupture termination and jump on parallel offset faults, *Bulletin of the Seismological Society of America* **98**, 440-447.

Olsen, K. B., and R. Takedatsu (2014). The SDSU Broadband Ground Motion Generation Module BBtoolbox Version 1.5, *Seismological Research Letters*, in review.

Onderdonk, N. W., T. K. Rockwell, S. F. McGill, and G. I. Marliyani (2013). Evidence for seven surface ruptures in the past 1600 years on the Claremont fault at Mystic Lake, northern San Jacinto fault zone, California, *Bulletin of the Seismological Society of America* **103**, 519-541.

Palmer, A. C., and J. R. Rice (1973). The growth of slip surfaces in the progressive failure of overconsolidated clay, *Proceedings of the Royal Society of London Series A* **332,** 527-548.

Park, S.K ., D. Pendergraft, W. J. Stephenson, K. M. Shedlock, T. C. Lee (1995). Delineation of intrabasin structure in a dilational jog of the San Jacinto fault zone, southern California, *Journal of Geophysical Research* **100***,* 691-702.

Petersen, M. D., A. D. Frankel, S. C. Harmsen, C. S. Mueller, K. M. Haller, R. L. Wheeler, R. L. Wesson, Y. Zeng, O. S. Boyd, D. M. Perkins, N. Luco, E. H. Field, C. J. Wills, and K. S. Rukstales (2008), Documentation for the 2008 Update of the United States National Seismic Hazard Maps, *U.S. Geological Survey Open-File Report* 2008–1128.

Petersen, M. D., M. P. Moschetti, P. M. Powers, C. S. Mueller, K. M. Haller, A. D. Frankel, Y. Zeng, S. Rezaeian, S. C. Harmsen, O. S. Boyd, E. H. Field, R. Chen, K. S. Rukstales, N. Luco, R. L. Wheeler, R. A. Williams, and A. H. Olsen (2014). Documentation for the 2014 update of the United States National Seismic Hazard Maps, *U.S. Geological Survey Open-File Report* 2014–1091

Plesch, A., J. H. Shaw, C. Benson, W. A. Bryant, S. Carena, M. Cooke, J. Dolan, G. Fuis, E. Gath, L. Grant, E. Hauksson, T. Jordan, M. Kamerling, M. Legg, S. Lindvall, H. Magistrale, C. Nicholson, N. Niemi, M. Oskin, S. Perry, G. Planansky, T. Rockwell, P. Shearer, C. Sorlien, M. P. Süss, J. Suppe, J. Treiman, and R. Yeats (2007). Community fault model (CFM) for Southern California, *Bulletin of the Seismological Society of America* **97**, 1793-1802.

Pullammanappallil, S.K., M.D. Purvance, and J.N. Brune (2006). Refraction microtremor (ReMi) results for Vs30 at precarious rock sites between the Elsinore and San Jacinto faults. 2006 SCEC Annual Meeting poster abstract; http://www.scec.org/meetings/2006am/index.html.

Purvance, M., J. Brune, N. A. Abrahamson, and J. G. Anderson (2008). Consistency of precariously balanced rocks with probabilistic seismic hazard estimates in southern California, *Bulletin of the Seismological Society of America* **98**, 2629-2640, doi: 10.1785/0120080169.

Rockwell, T. K., T. E. Dawson, J. Young, and G. Seitz (2014). A 21-event, 4000-year history of surface ruptures in the Anza seisic gap, San Jacinto fault and implications for long-term earthquake production on a major plate boundary fault, *Pure and Applied Geophysics*, in press.

Salisbury, J. B., T. K. Rockwell, T. J. Middleton, and K. W. Hudnut (2012). LiDAR and field observations of slip distribution for the most recent surface ruptures along the central San Jacinto fault, *Bulletin of the Seismological Society of America* **102**, 598–619.

Sanders, C.O., and H. Kanamori (1994). A seismotectonic analysis of the Anza seismic gap, San Jacinto fault zone, southern California, *Journal of Geophysical Research* **89**, 5873-5890.

Toppazada, T., D. Branum, M. Reichle, and C. Hallstrom (2002). San Andreas fault zone, California: M ≥5:5 earthquake history, *Bulletin of the Seismological Society of America* **92**, 2555–2601.

U.S. Geological Survey and California Geological Survey (2010). *Quaternary fault and fold database for the United States*.

Wells, D. L., and K. J. Coppersmith (1994). New empirical relationships among magnitude, rupture length, rupture width, rupture area, and surface displacement, *Bulletin of the Seismological Society of America* **84**, 974-1002.

Wesnousky, S. G. (2008). Displacement and geometrical characteristics of earthquake surface ruptures: issues and implications for seismic-hazard analysis and the process of earthquake rupture, *Bulletin of the Seismological Society of America* **98**, 1609-1632.

Zeng, Y. H., K. Aki, and T. L. Teng (1993). Mapping of the high-frequency source radiation for the Loma Prieta earthquake, California, *Journal of Geophysical Research* **98**, no. B7, 11981-11993.

Zeng, Y. H. F. Su, and K. Aki (1991). Scattering wave energy propagation in a random isotropic scattering medium 1. Theory, *Journal of Geophysical Research* **96**, no. B1, 607-619.

Tables

Table 1. List of PBRs included in analysis

Precariously Balanced Rocks		Coordinates In Mesh	a_1 in degrees	a_2 in degrees
001-btr	Benton Road	-116.9280129, 33.592667752	11	19
002-gv01	gv01	-117.24549918, 34.277363353	29	36
003-mvt	Mead Valley tipped	-117.25763844, 33.817393437	29	28
004-motte1	motte1_rock	-117.25764160, 33.812388117	8	17
005-gv05	gv05	-117.24852457, 34.279944432	20	20
006-sw01	sw01	-117.34152371, 34.295536945	15	--
007-motte2	Motte2	-117.25765807, 33.80236931	9	24.12
008-spd	S. of Perris Dam	-117.18652296, 33.824575788	15	46.1
009-lvm	Lakeview Mountains	-117.07105234, 33.772392190	21.4	44.7
010-pvlm	Pulsar View Lakeview Mtn	-117.08314105, 33.817631772	13	21
011-mvm	Mead Valley mushroom	-117.26375373, 33.822477414	21.88	23.37
012-gpg	Gopher Gulch	-117.36460956, 33.901433630	22.79	24.58
013-lpn	Lake Perris North	-117.16486992, 33.886957443	11	31
014-ucr	UCR	-117.31776094, 33.964182478	25	35
015-sj08	sj08	-116.98565252, 33.895716821	21	21
016-sj06	sj06	-116.98246022, 33.898270027	--	--
017-sj05	sj05	-116.98993160, 33.902274440	12	32
018-sj04	sj04	-116.99280445, 33.904966854	15	26
019-sj02	sj02	-117.00532429, 33.894950876	16	28
020-sj07	sj07	-116.89780871, 33.898982263	32	32

Table 2. Horizontal PGAs (g) at the PBRs for the 4 scenarios.

	A1		B2		C1		D2	
Stations	NS	EW	NS	EW	NS	EW	NS	EW
001-btr	0.10	0.11	0.086	0.097	0.19	0.20	0.11	0.088
002-gv01	0.17	0.14	0.12	0.19	0.099	0.086	0.15	0.16
003-mvt	0.30	0.22	0.19	0.21	0.42	0.39	0.16	0.16
004-motte1	0.13	0.18	0.28	0.34	0.16	0.13	0.27	0.19
005-gv05	0.078	0.086	0.18	0.20	0.13	0.10	0.17	0.24
006-sw01	0.14	0.18	0.10	0.11	0.088	0.059	0.16	0.12
007-motte2	0.30	0.22	0.19	0.20	0.20	0.17	0.20	0.18
008-spd	0.29	0.34	0.42	0.25	0.42	0.45	0.19	0.25
009-lvm	0.20	0.20	0.27	0.18	0.32	0.24	0.13	0.11
010-pvlm	0.23	0.22	0.27	0.33	0.57	0.55	0.17	0.27
011-mvm	0.29	0.20	0.18	0.11	0.20	0.22	0.26	0.19
012-gpg	0.33	0.33	0.20	0.18	0.19	0.16	0.28	0.25
013-lpn	0.27	0.27	0.39	0.37	0.57	0.56	0.27	0.40
014-ucr	0.31	0.26	0.21	0.20	0.21	0.19	0.52	0.53
015-sj08	0.25	0.33	0.32	0.29	0.65	0.41	0.18	0.14
016-sj06	0.25	0.30	0.45	0.35	0.40	0.41	0.28	0.11
017-sj05	0.16	0.15	0.33	0.26	0.76	0.67	0.39	0.47
018-sj04	0.30	0.28	0.23	0.35	0.34	0.66	0.34	0.22
019-sj02	0.18	0.25	0.24	0.24	0.57	0.44	0.28	0.20
020-sj07	0.16	0.19	0.20	0.18	0.40	0.33	0.20	0.15

Table 3. Horizontal SA-1s (g) values at the PBRs for the 4 scenarios.

	A1		B2		C1		D2	
Stations	NS	EW	NS	EW	NS	EW	NS	EW
001-btr	0.061	0.078	0.055	0.050	0.092	0.101	0.049	0.046
002-gv01	0.077	0.066	0.085	0.10	0.19	0.15	0.12	0.11
003-mvt	0.14	0.083	0.10	0.089	0.18	0.20	0.091	0.094
004-motte1	0.077	0.094	0.17	0.15	0.096	0.081	0.096	0.098
005-gv05	0.051	0.046	0.087	0.083	0.20	0.16	0.15	0.13
006-sw01	0.078	0.076	0.067	0.096	0.13	0.048	0.12	0.13
007-motte2	0.15	0.085	0.12	0.079	0.14	0.10	0.097	0.077
008-spd	0.14	0.17	0.18	0.091	0.21	0.24	0.085	0.086
009-lvm	0.12	0.12	0.12	0.081	0.26	0.13	0.11	0.072
010-pvlm	0.11	0.14	0.14	0.17	0.25	0.33	0.13	0.14
011-mvm	0.11	0.10	0.11	0.052	0.13	0.13	0.12	0.080
012-gpg	0.15	0.14	0.14	0.12	0.25	0.19	0.27	0.22
013-lpn	0.12	0.15	0.21	0.20	0.33	0.31	0.15	0.19
014-ucr	0.15	0.14	0.18	0.12	0.24	0.24	0.28	0.33
015-sj08	0.26	0.19	0.25	0.18	0.28	0.28	0.17	0.099
016-sj06	0.24	0.22	0.29	0.15	0.16	0.25	0.19	0.090
017-sj05	0.18	0.16	0.26	0.19	0.36	0.38	0.22	0.19
018-sj04	0.21	0.20	0.24	0.20	0.19	0.37	0.22	0.16
019-sj02	0.21	0.23	0.30	0.20	0.29	0.34	0.27	0.17
020-sj07	0.22	0.19	0.22	0.14	0.21	0.21	0.17	0.10

Table 4. Horizontal PGVs (m/s) at the PBRs for the 4 scenarios.

	A1		B2		C1		D2	
Stations	NS	EW	NS	EW	NS	EW	NS	EW
001-btr	0.060	0.085	0.072	0.064	0.10	0.13	0.053	0.056
002-gv01	0.10	0.10	0.10	0.12	0.18	0.14	0.15	0.12
003-mvt	0.19	0.15	0.15	0.090	0.22	0.24	0.14	0.091
004-motte1	0.12	0.14	0.21	0.17	0.15	0.11	0.15	0.11
005-gv05	0.085	0.078	0.12	0.12	0.18	0.14	0.17	0.15
006-sw01	0.11	0.11	0.088	0.10	0.20	0.13	0.18	0.17
007-motte2	0.17	0.15	0.16	0.11	0.16	0.12	0.14	0.093
008-spd	0.19	0.22	0.24	0.16	0.25	0.27	0.12	0.14
009-lvm	0.13	0.15	0.23	0.15	0.17	0.20	0.18	0.070
010-pvlm	0.13	0.18	0.26	0.30	0.30	0.34	0.13	0.20
011-mvm	0.19	0.16	0.16	0.064	0.18	0.14	0.15	0.095
012-gpg	0.20	0.21	0.22	0.15	0.30	0.16	0.28	0.20
013-lpn	0.20	0.27	0.43	0.21	0.32	0.37	0.26	0.25
014-ucr	0.30	0.17	0.27	0.15	0.36	0.23	0.37	0.40
015-sj08	0.30	0.24	0.32	0.37	0.28	0.33	0.32	0.11
016-sj06	0.27	0.22	0.42	0.30	0.24	0.34	0.32	0.11
017-sj05	0.25	0.20	0.36	0.34	0.38	0.41	0.34	0.27
018-sj04	0.27	0.26	0.29	0.35	0.23	0.45	0.33	0.19
019-sj02	0.25	0.23	0.35	0.43	0.33	0.36	0.37	0.18
020-sj07	0.27	0.17	0.27	0.31	0.28	0.30	0.33	0.15

Figure Captions

Figure 1. Map of the San Jacinto Fault Zone, with a geometry based on the USGS Quaternary Faults Database (USGS, 2010). The Claremont strand is shown in blue, the Farm Road strand in red, and the Casa Loma-Clark strand in black. Other strands of the SJF are shown in yellow, and other Quaternary faults are shown in gray. Cities are indicated with blue dots. The area of the present study is enclosed in the green box.

Figure 2. Map of the northern San Jacinto Fault, from Cajon Pass (NW corner of this map) to Anza (SE corner). The blue trace depicts the Claremont strand, red trace is the Farm Road strand, and the black trace is the Casa Loma strand. The stars depict the epicenters of the four rupture scenarios for which broadband seismograms were calculated. The triangles mark the 20 precariously balanced rocks sites described in this study (Table 1).

Figure 3. Mesh of the San Jacinto Fault, generated with FaultMod (Barall, 2009), as used in our dynamic models. The parts of the fault that are able to rupture are marked in white. The Claremont strand is to the upper left in this figure, the Casa Loma to the lower right, and the Farm Road is between them. The grid size is 100 m in the near field, and 400 m in the far field.

Figure 4. Four combined regional and stochastic shear stress realizations. The irregular patches are stochastic asperities, and the vertical banding is contributed by the regional stress field. Note that the normal stress field is purely regional, and lacks the asperities shown here. The lettered white dots on each plot are the forced nucleation points for our dynamic models. The dots with the black centers are the nucleation points that produced the largest ruptures; these are the ones we used to produce full broadband synthetic seismograms.

Figure 5. Fragility curves for PBR sites LPN (top), located to the SW of the San Jacinto Fault; SJ05 (center), located between the SJF and the San Andreas Fault; and GV05 (bottom), located in the San Bernardino Mountains. Probabilities are from 0 to 1. See Figure 2 for the PBR locations.

Figure 6. Plots of total horizontal slip for the four largest events – each is M6.9 – out of the set of sixteen total dynamic rupture models. The forced initial nucleation point in each is indicated by the black dot. These are the models we used to produce the low-frequency ground motions used as inputs for the hybrid broadband method.

Appendix A. Plots of total horizontal slip for the twelve dynamic rupture models that were not used to generate broadband synthetic seismograms. The black dot in each plot represents the nucleation point, depicted on Fig. 4 of the main text.

Appendix B. Plots of synthetic broadband accelerograms at the 20 PBR sites for all four rupture scenarios (1 stochastic realization), and comparisons between PGAs and SA-1s values for BBs and leading GMPEs.

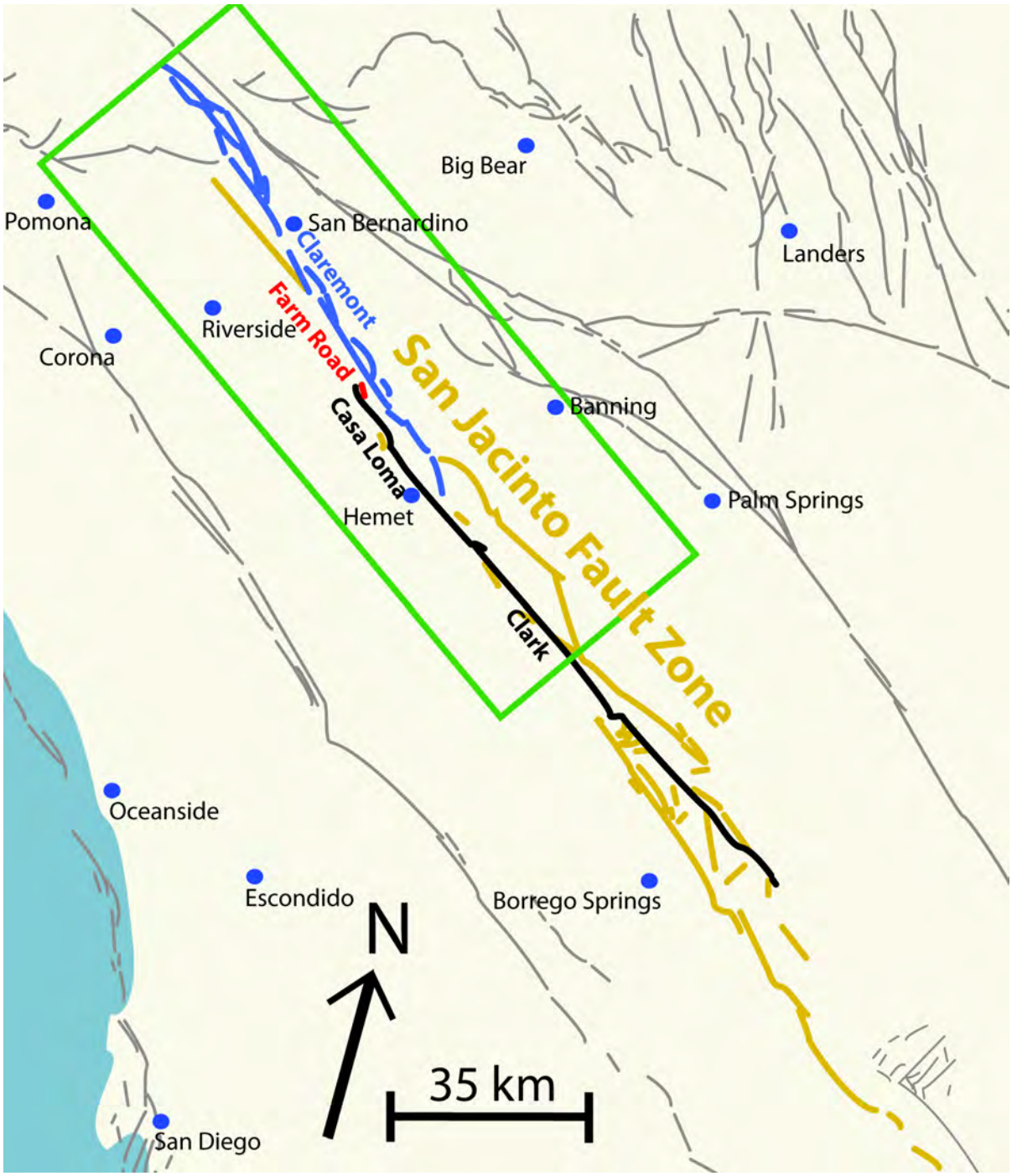
Big Bear
Pomona
San Bernardino
Landers
Claremont
Farm Road
Riverside
Corona
San Jacinto Fault Zone
Banning
Casa Loma
Hemet
Palm Springs
Clark
Oceanside
Escondido
Borrego Springs
N
35 km
San Diego

Figure 1.

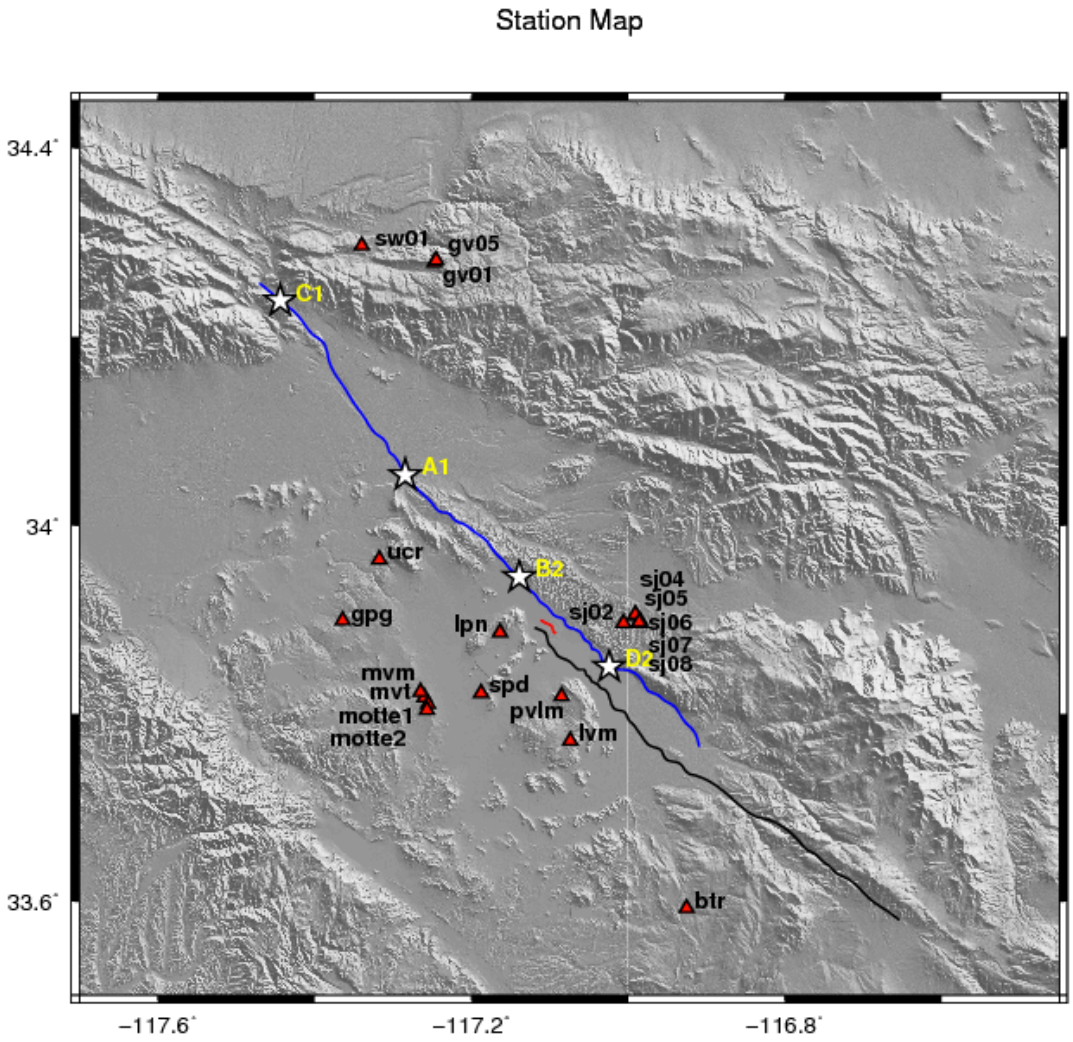
Station Map
34.4°
34°
33.6°
−117.6°
−117.2°
−116.8°
sw01
gv05
gv01
C1
A1
ucr
B2
sj04
sj05
sj02
sj06
sj07
sj08
gpg
lpn
D2
mvm
mvt
motte1
motte2
spd
pvlm
lvm
btr

Figure 2.

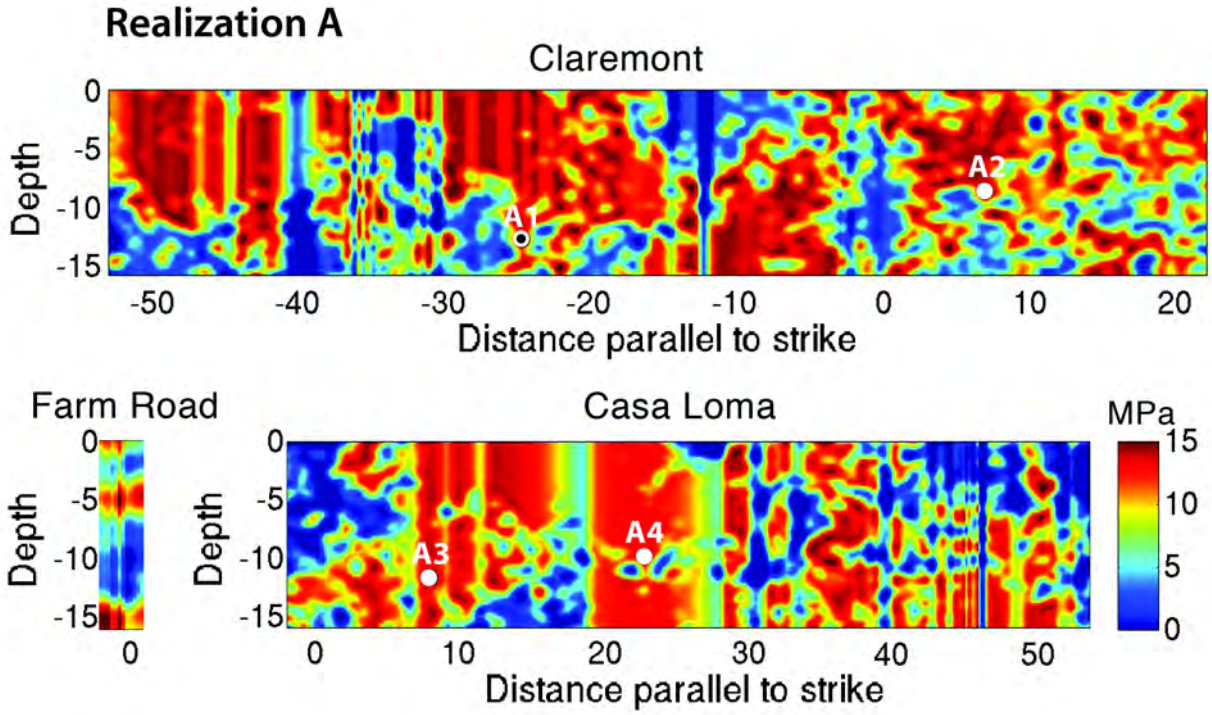
Realization A
Claremont
Depth
0
-5
-10
-15
A1
A2
-50
-40
-30
-20
-10
0
10
20
Distance parallel to strike
Farm Road
Casa Loma
MPa
15
10
5
0
A3
A4
0
10
20
30
40
50
Distance parallel to strike

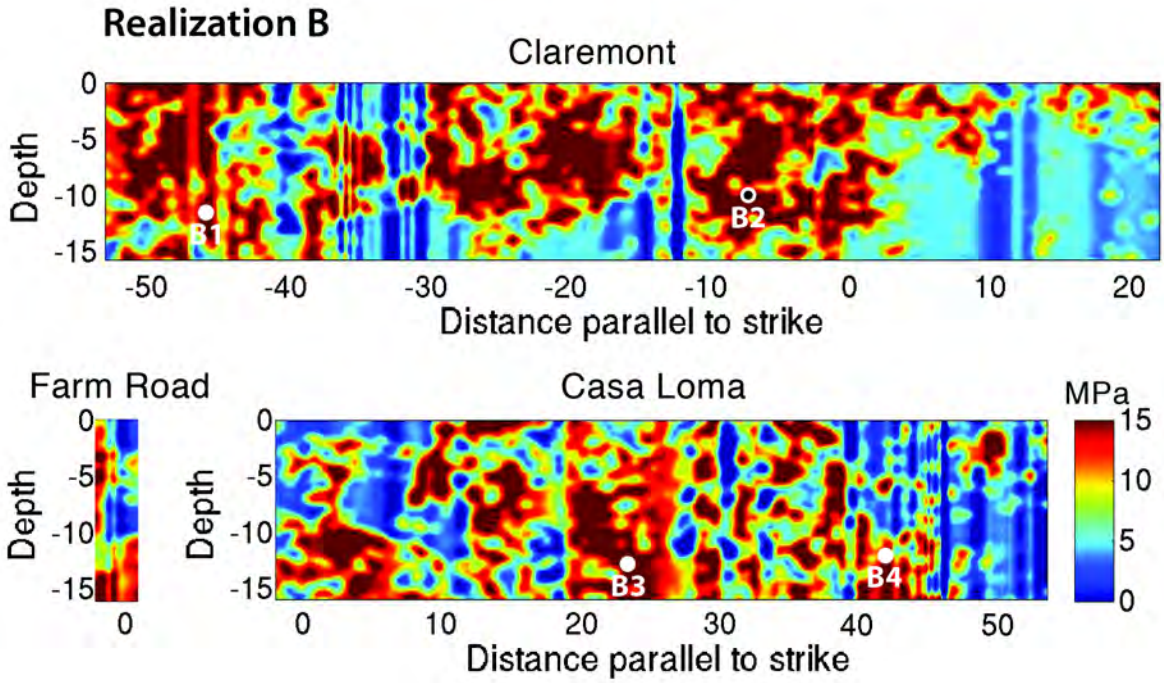
Realization B
Claremont
Depth
0
-5
-10
-15
B1
B2
-50
-40
-30
-20
-10
0
10
20
Distance parallel to strike
Farm Road
Casa Loma
MPa
15
10
5
0
B3
B4
0
10
20
30
40
50
Distance parallel to strike

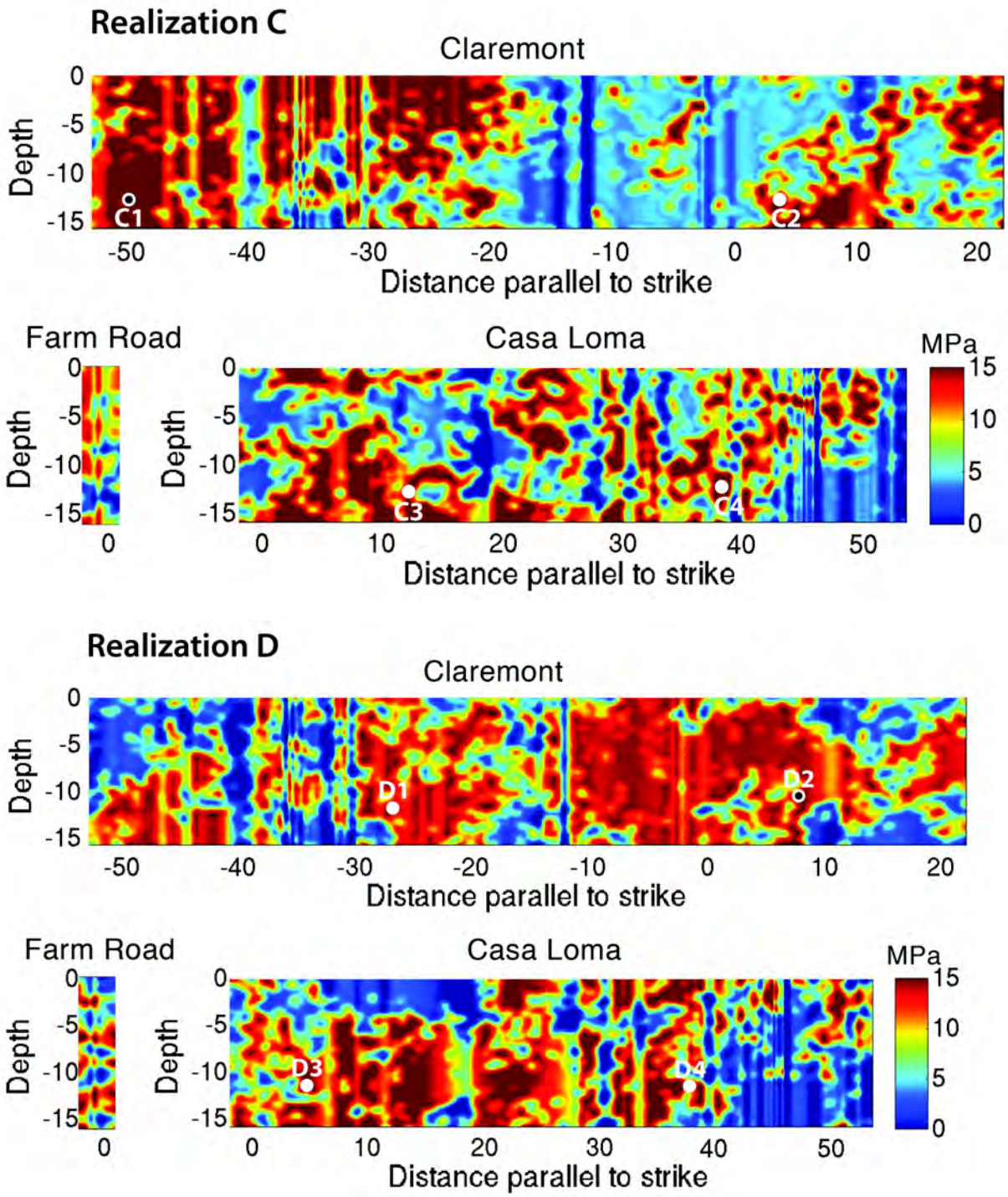
Realization C
Claremont
Depth
0
-5
-10
-15
C1
C2
-50
-40
-30
-20
-10
0
10
20
Distance parallel to strike
Farm Road
Casa Loma
MPa
15
10
5
0
C3
C4
0
10
20
30
40
50
Distance parallel to strike
Realization D
Claremont
D1
D2
Distance parallel to strike
Farm Road
Casa Loma
D3
D4
Distance parallel to strike

Figure 4.

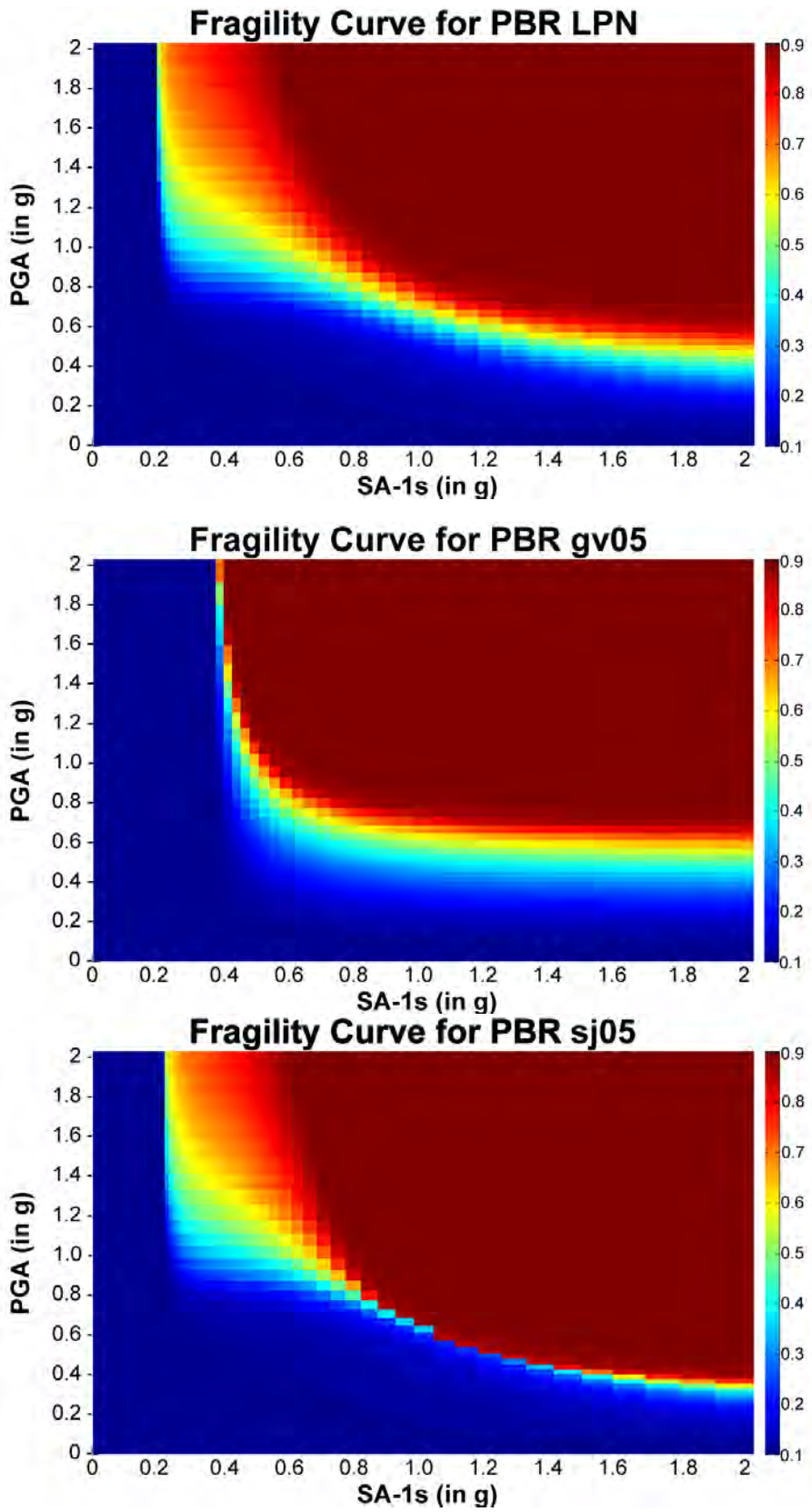
Fragility Curve for PBR LPN
PGA (in g)
SA-1s (in g)
Fragility Curve for PBR gv05
PGA (in g)
SA-1s (in g)
Fragility Curve for PBR sj05
PGA (in g)
SA-1s (in g)

Figure 5.

Total Horizontal Slip - Model A1

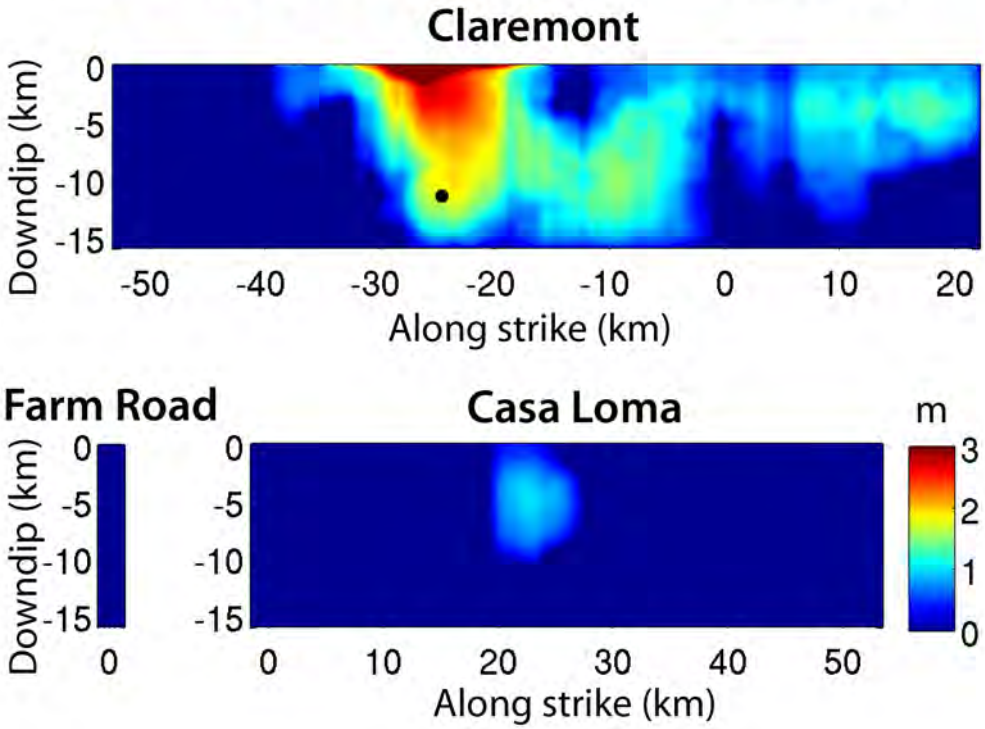

Total Horizontal Slip - Model B2

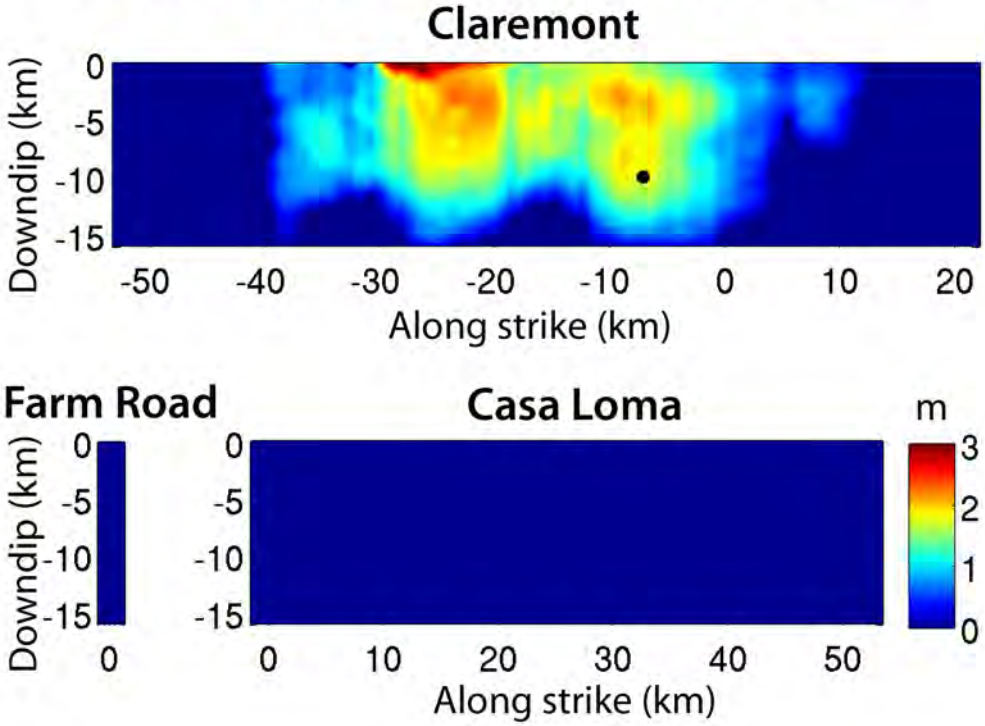

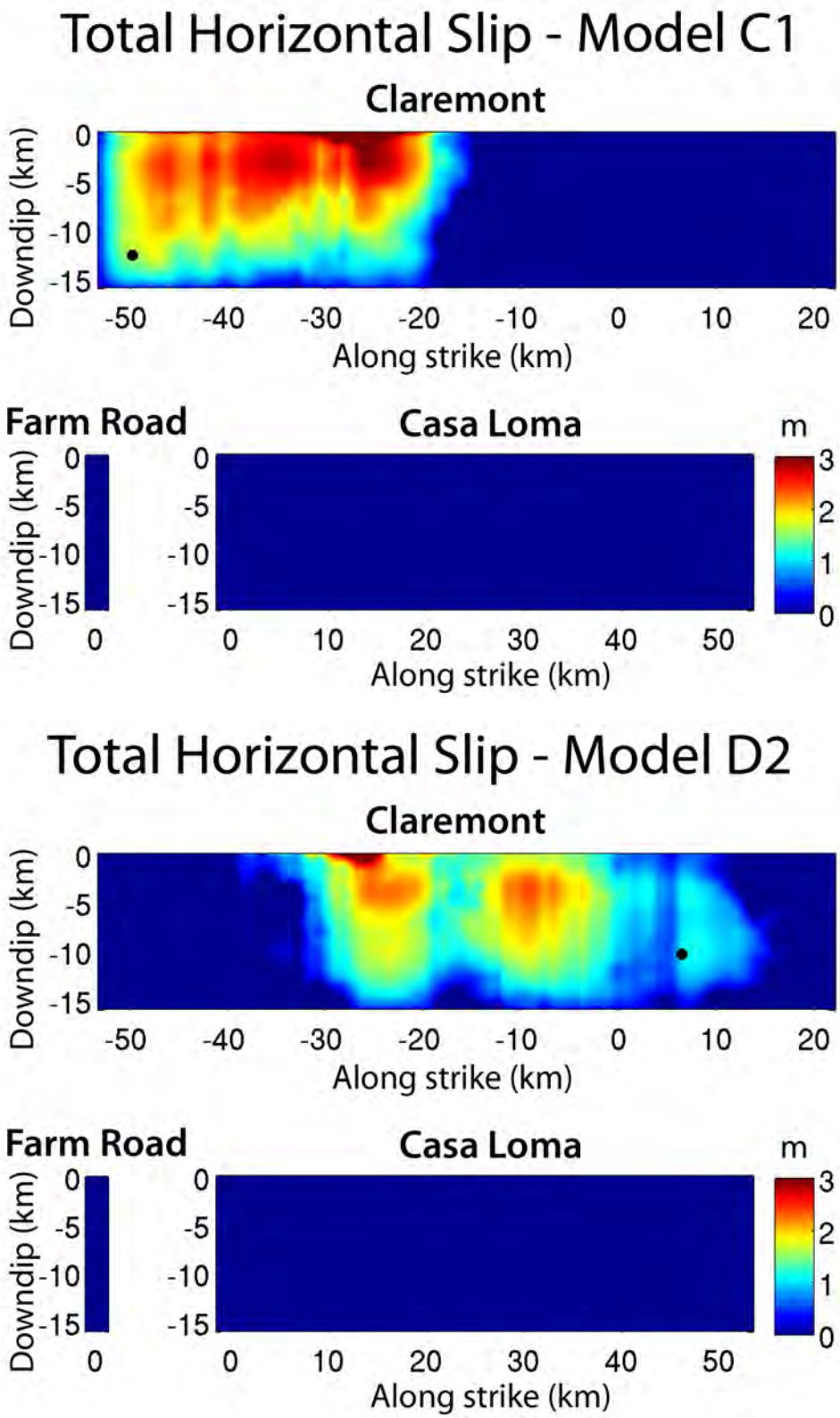
Total Horizontal Slip - Model C1
Claremont
Downdip (km)
0
-5
-10
-15
-50
-40
-30
-20
-10
0
10
20
Along strike (km)
Farm Road
Casa Loma
m
3
2
1
0
Total Horizontal Slip - Model D2
Claremont
Farm Road
Casa Loma

Figure 6.

Appendix A.

Plots of total horizontal slip for the twelve dynamic rupture models that were not used to generate broadband synthetic seismograms. The black dot in each plot represents the nucleation point, depicted on Fig. 4 of the main text.

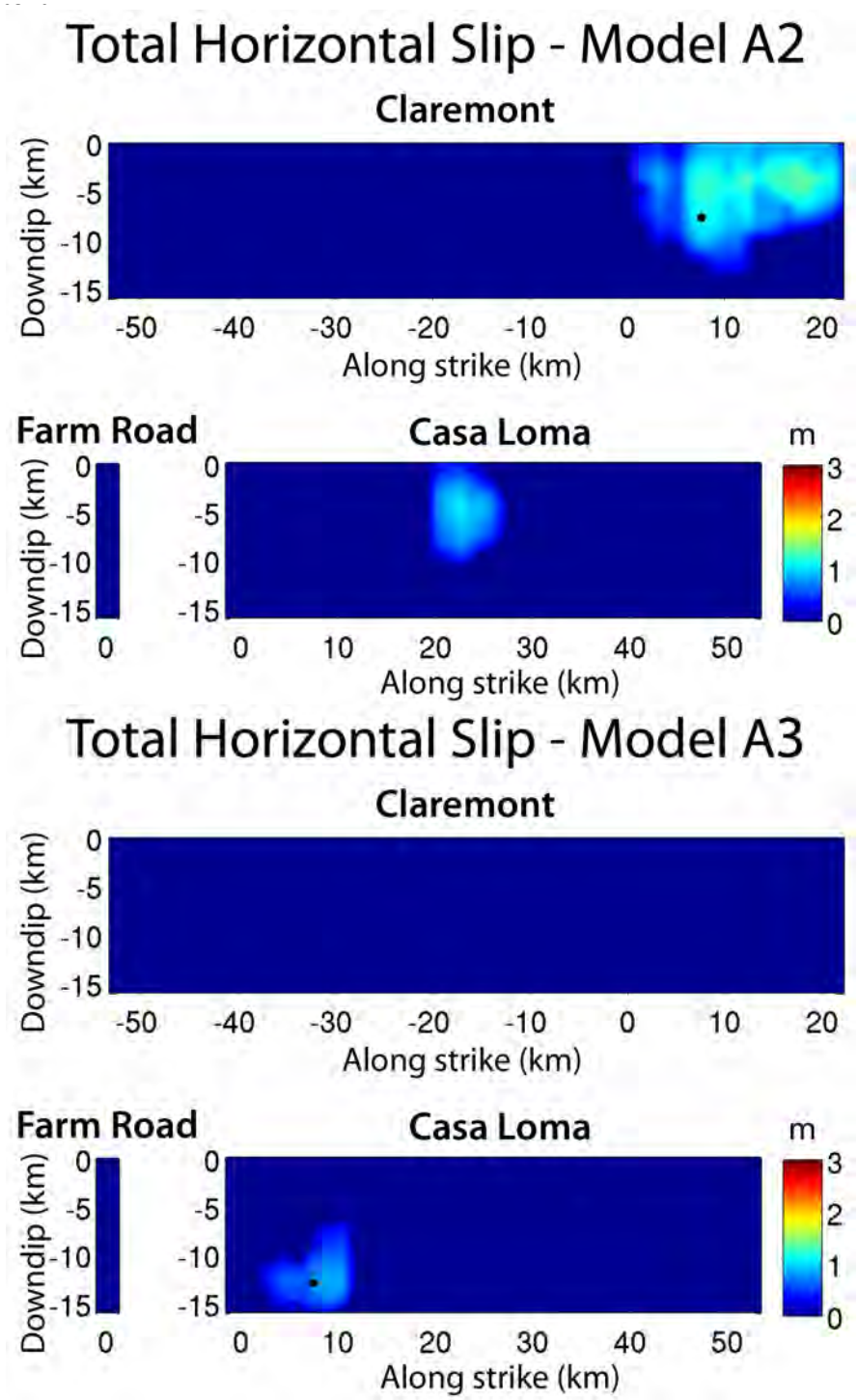

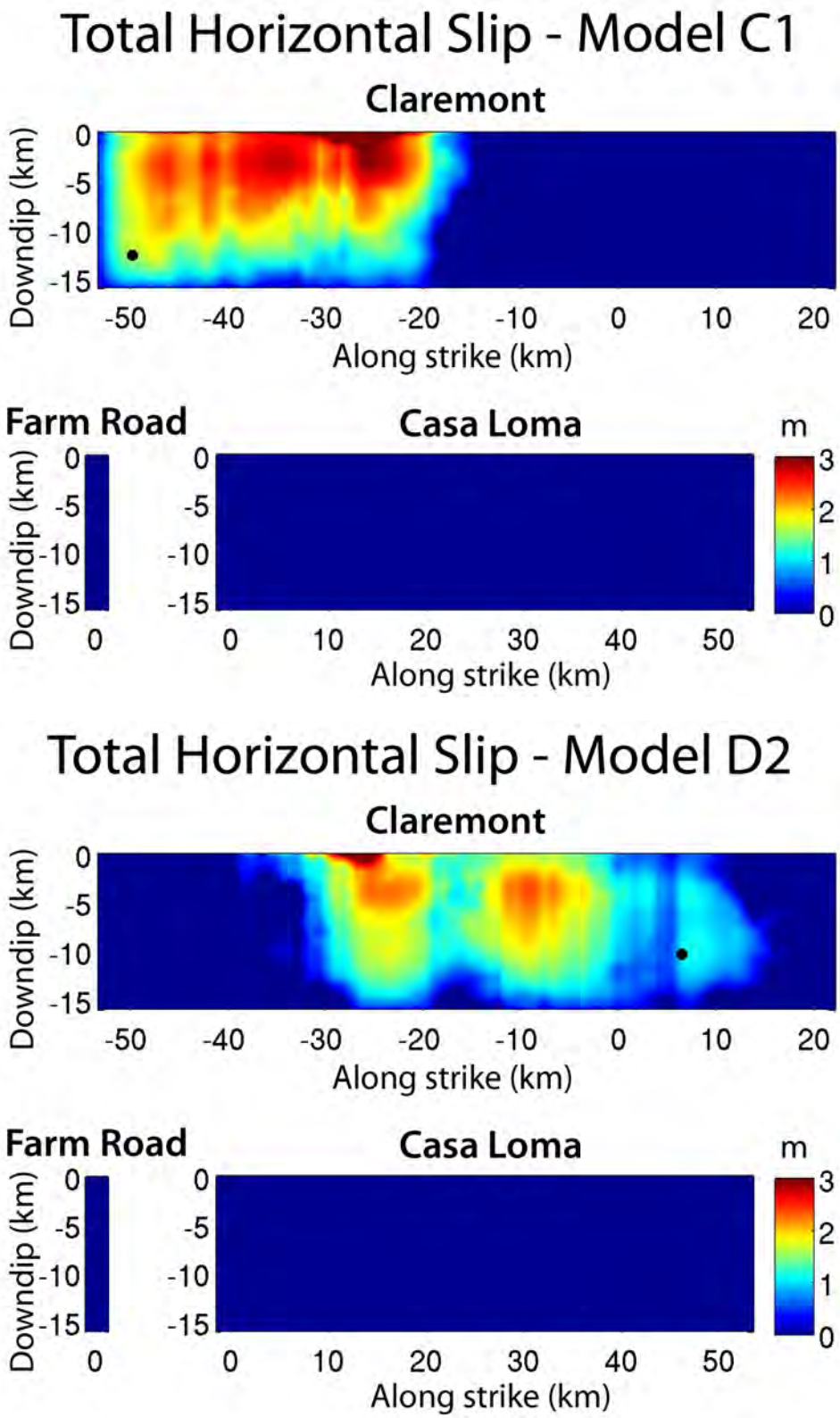
Total Horizontal Slip - Model C1
Claremont
Downdip (km)
0
-5
-10
-15
-50
-40
-30
-20
-10
0
10
20
Along strike (km)
Farm Road
Casa Loma
m
3
2
1
0
Total Horizontal Slip - Model D2
Claremont
Farm Road
Casa Loma

Figure 6.

Appendix A.

Plots of total horizontal slip for the twelve dynamic rupture models that were not used to generate broadband synthetic seismograms. The black dot in each plot represents the nucleation point, depicted on Fig. 4 of the main text.

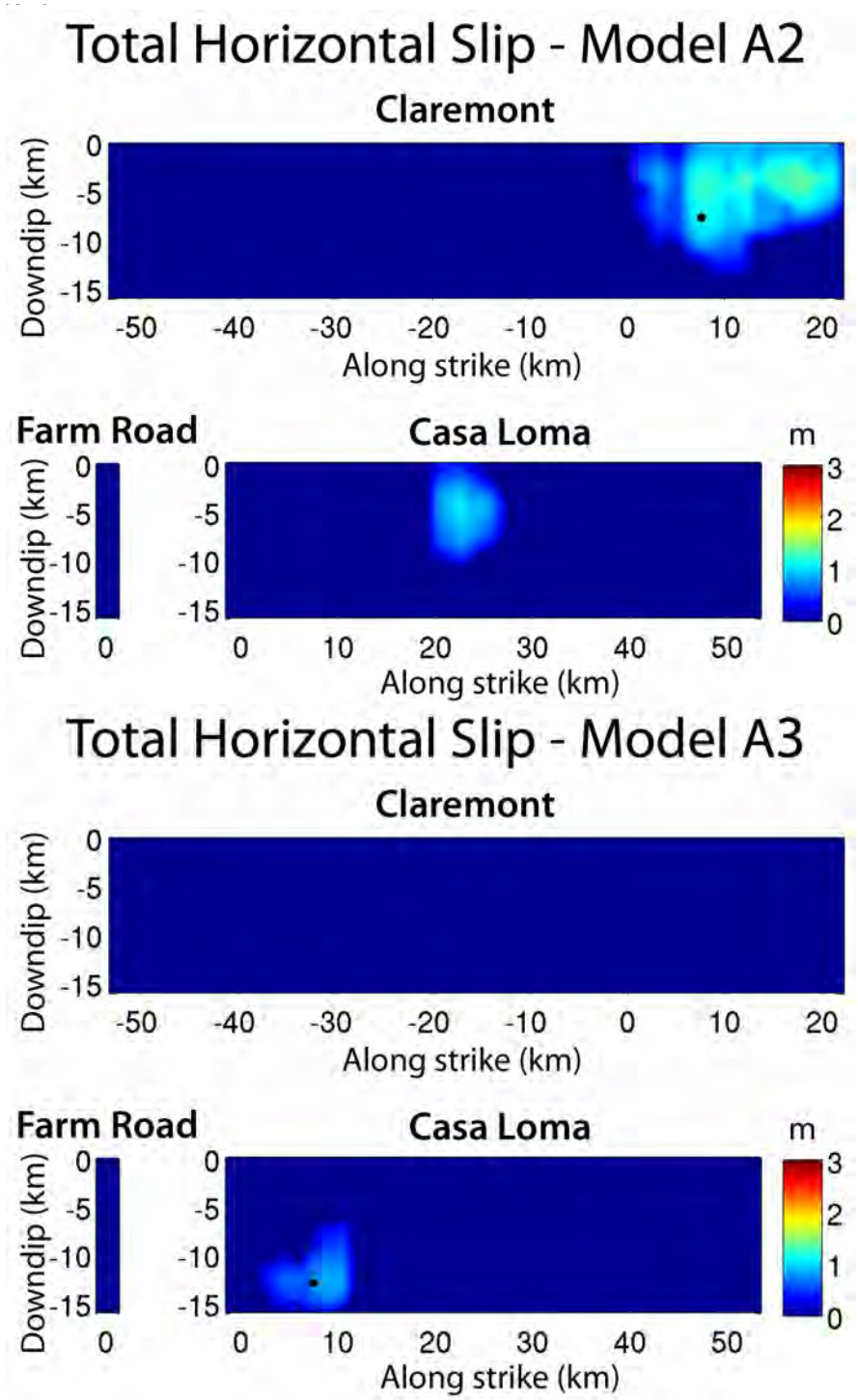

Total Horizontal Slip - Model A4

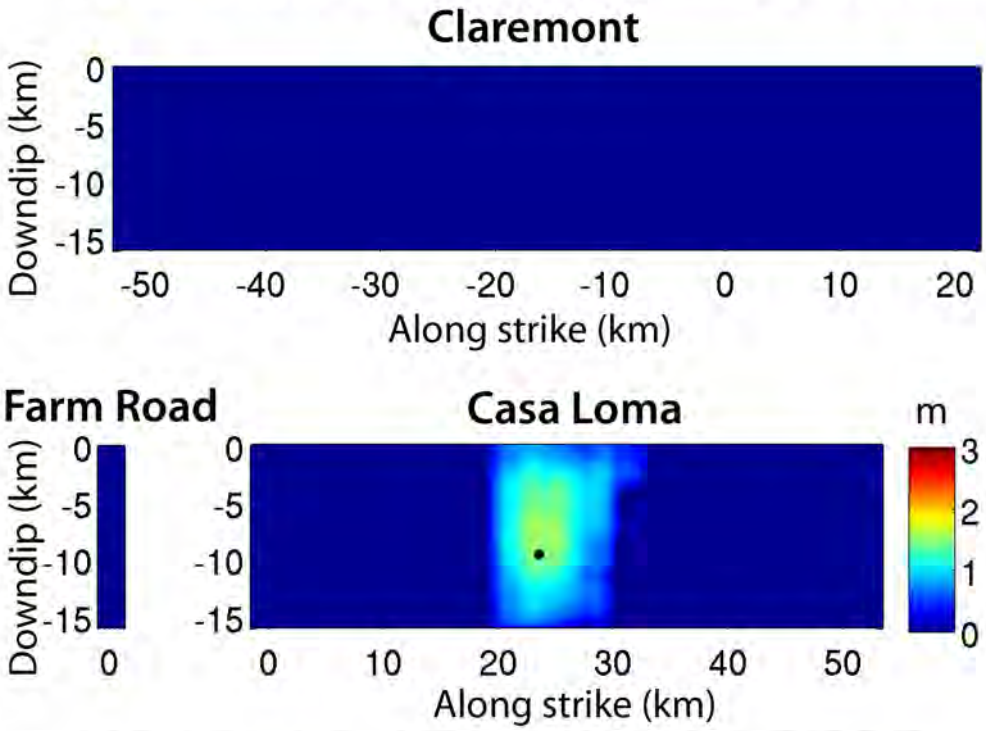

Total Horizontal Slip - Model B1

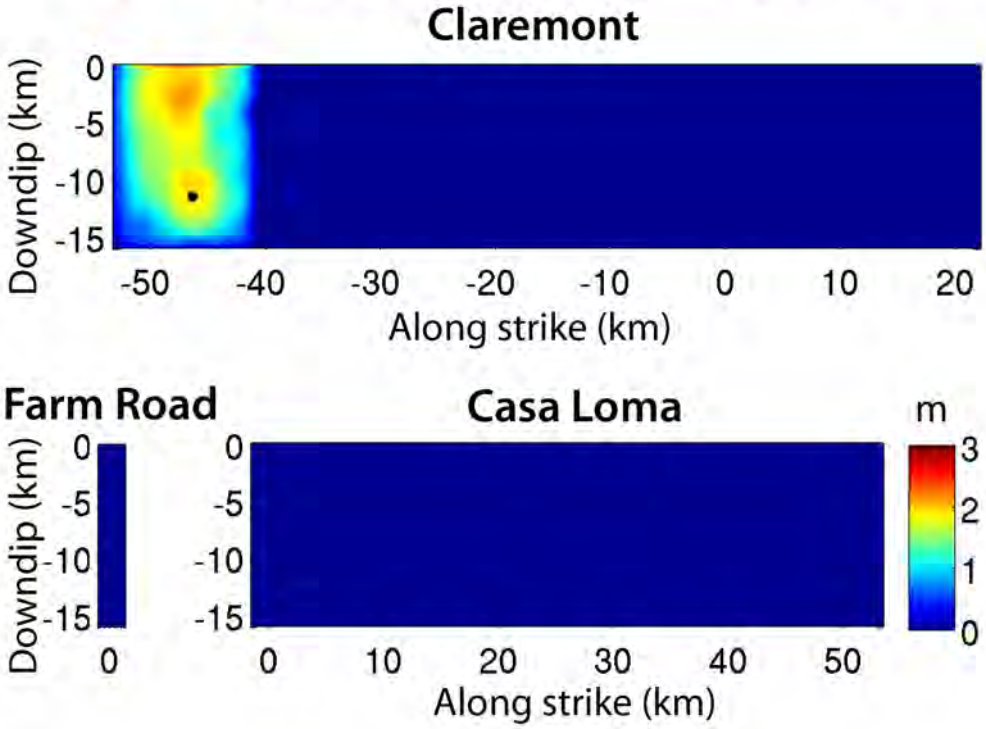

Total Horizontal Slip - Model B3

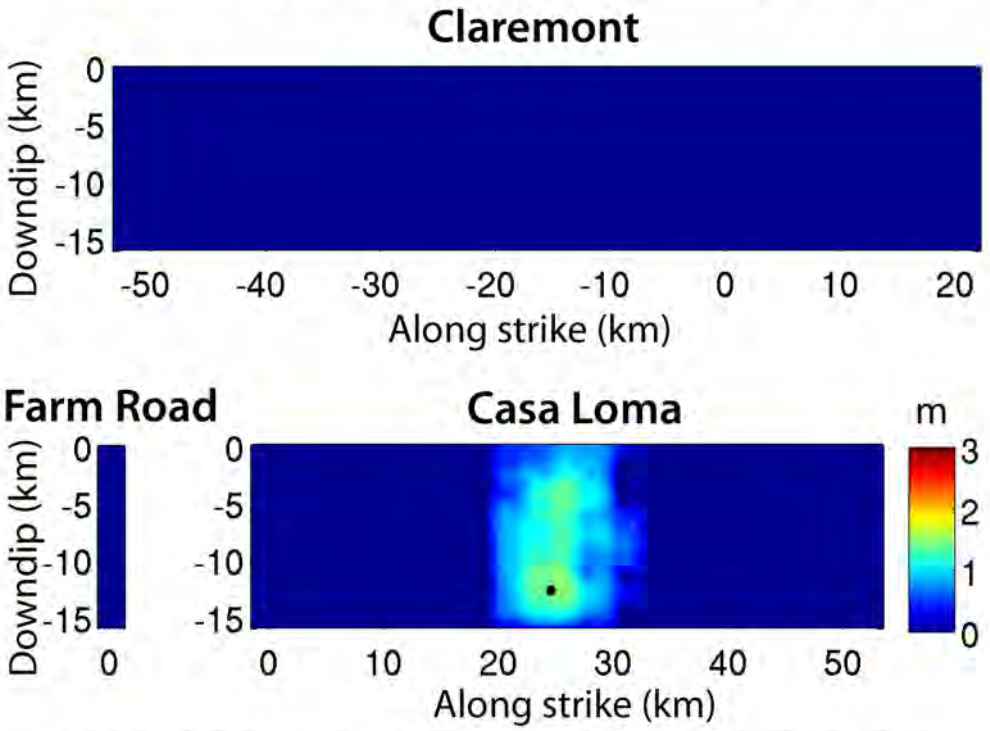

Total Horizontal Slip - Model B4

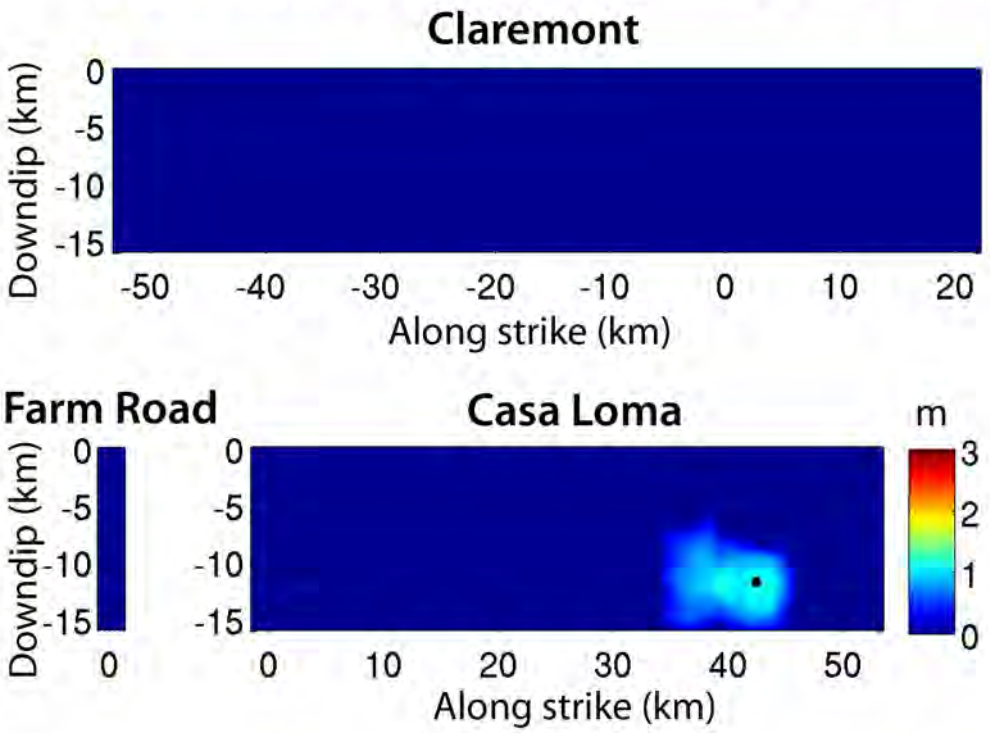

Total Horizontal Slip - Model C2

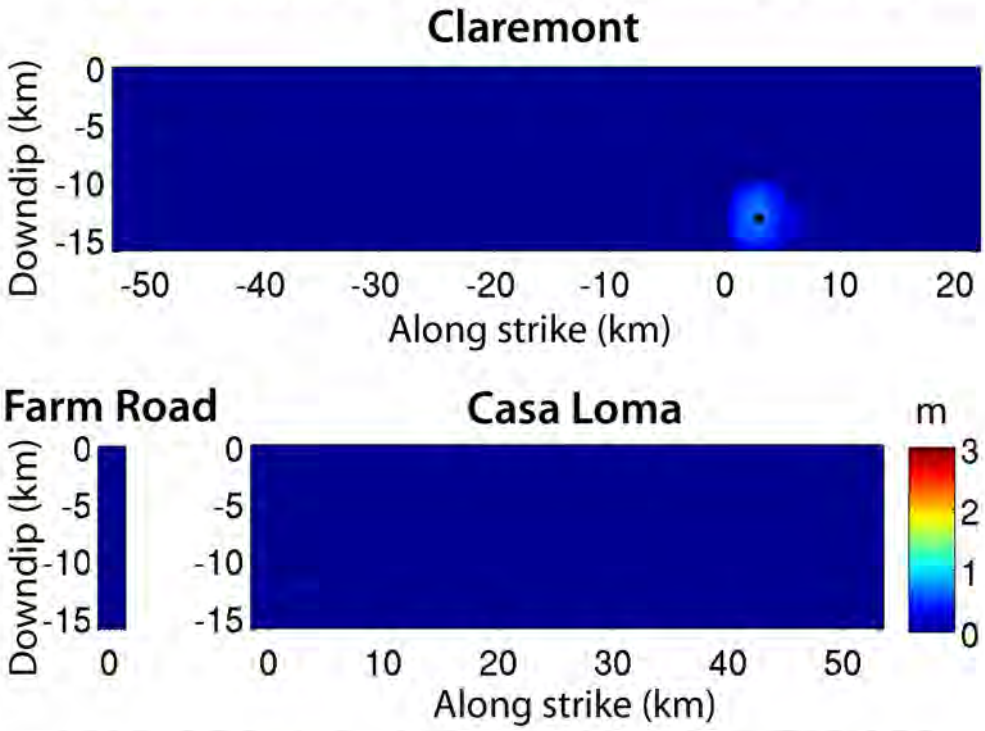

Total Horizontal Slip - Model C3

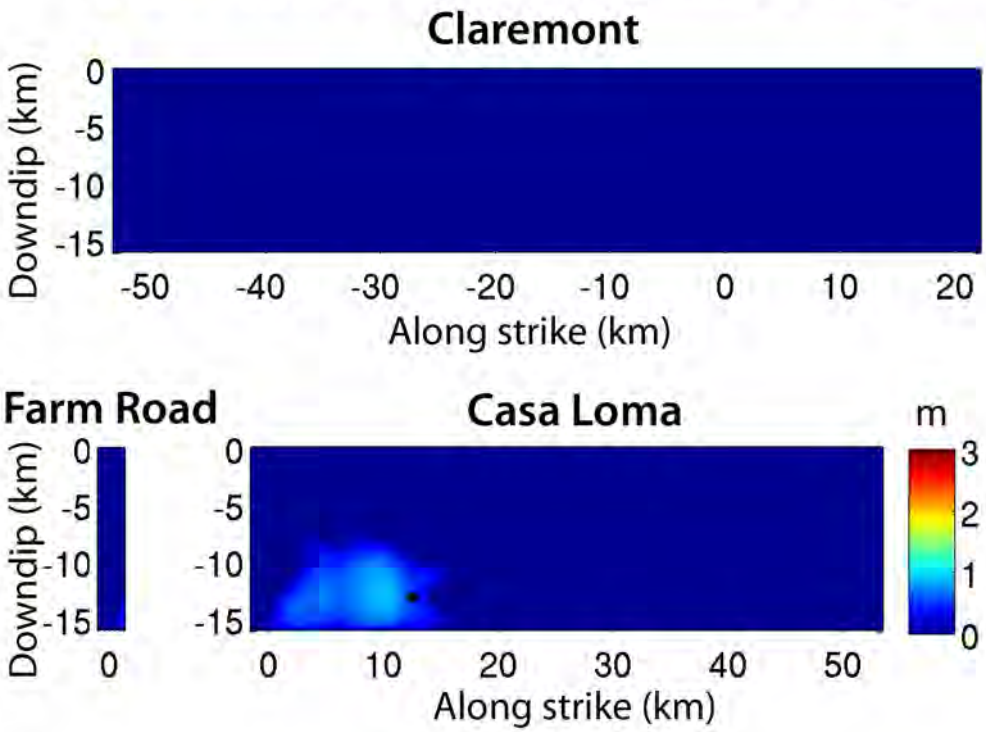

Total Horizontal Slip - Model C4

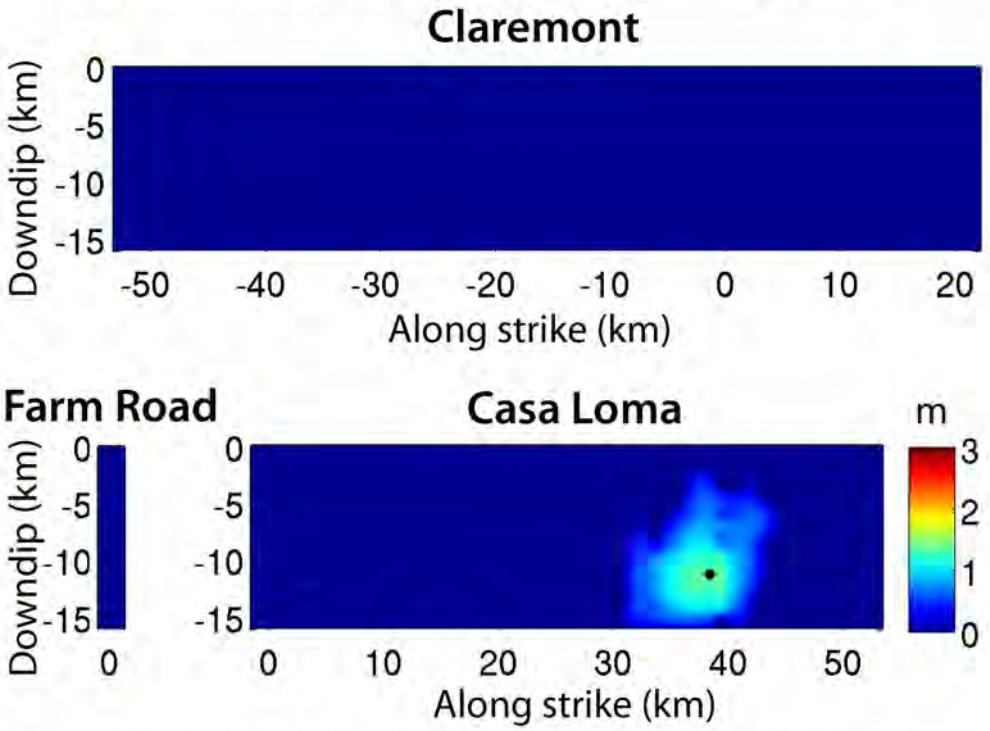

Total Horizontal Slip - Model D1

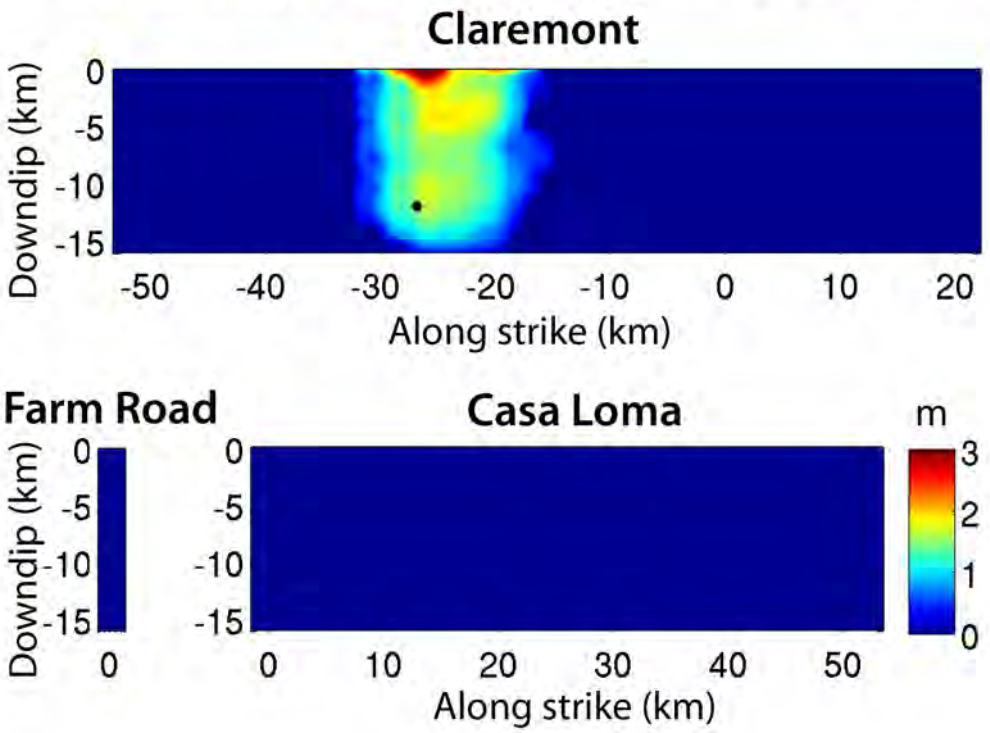

Total Horizontal Slip - Model D3

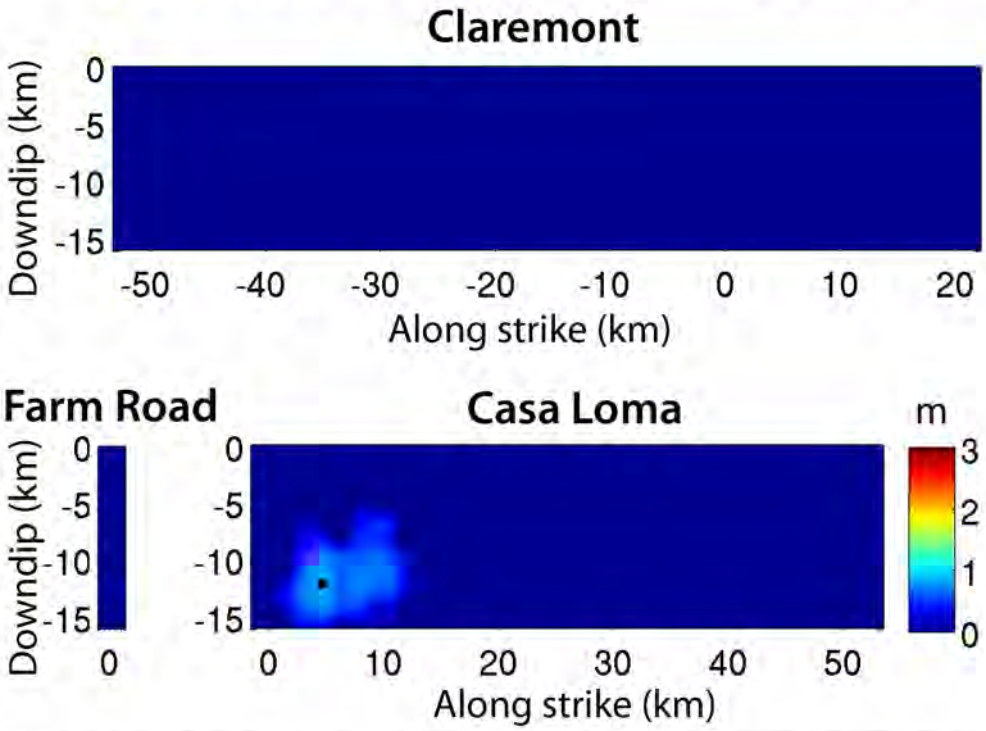

Total Horizontal Slip - Model D4

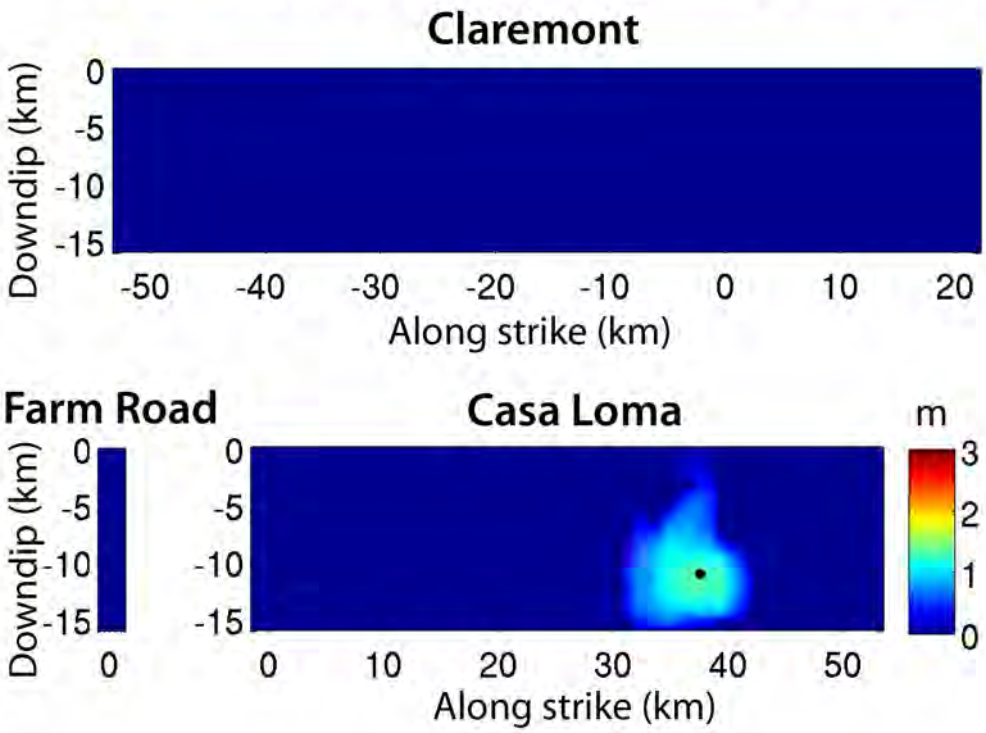

Appendix B.

Plots of synthetic broadband accelerograms at the 20 PBR sites for all four rupture scenarios (1 stochastic realization), and comparisons between PGAs and SA-1s values for BBs and leading GMPEs.

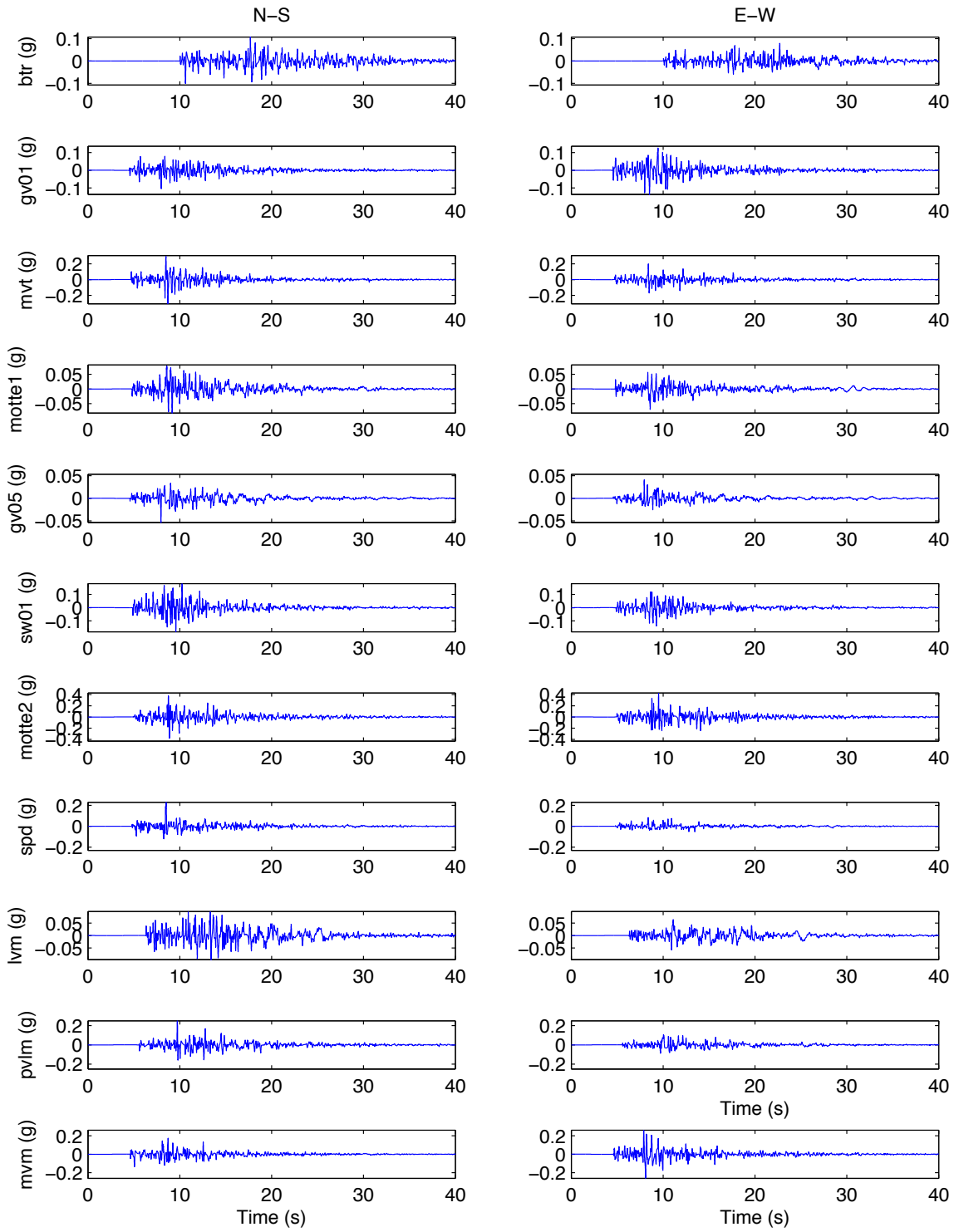

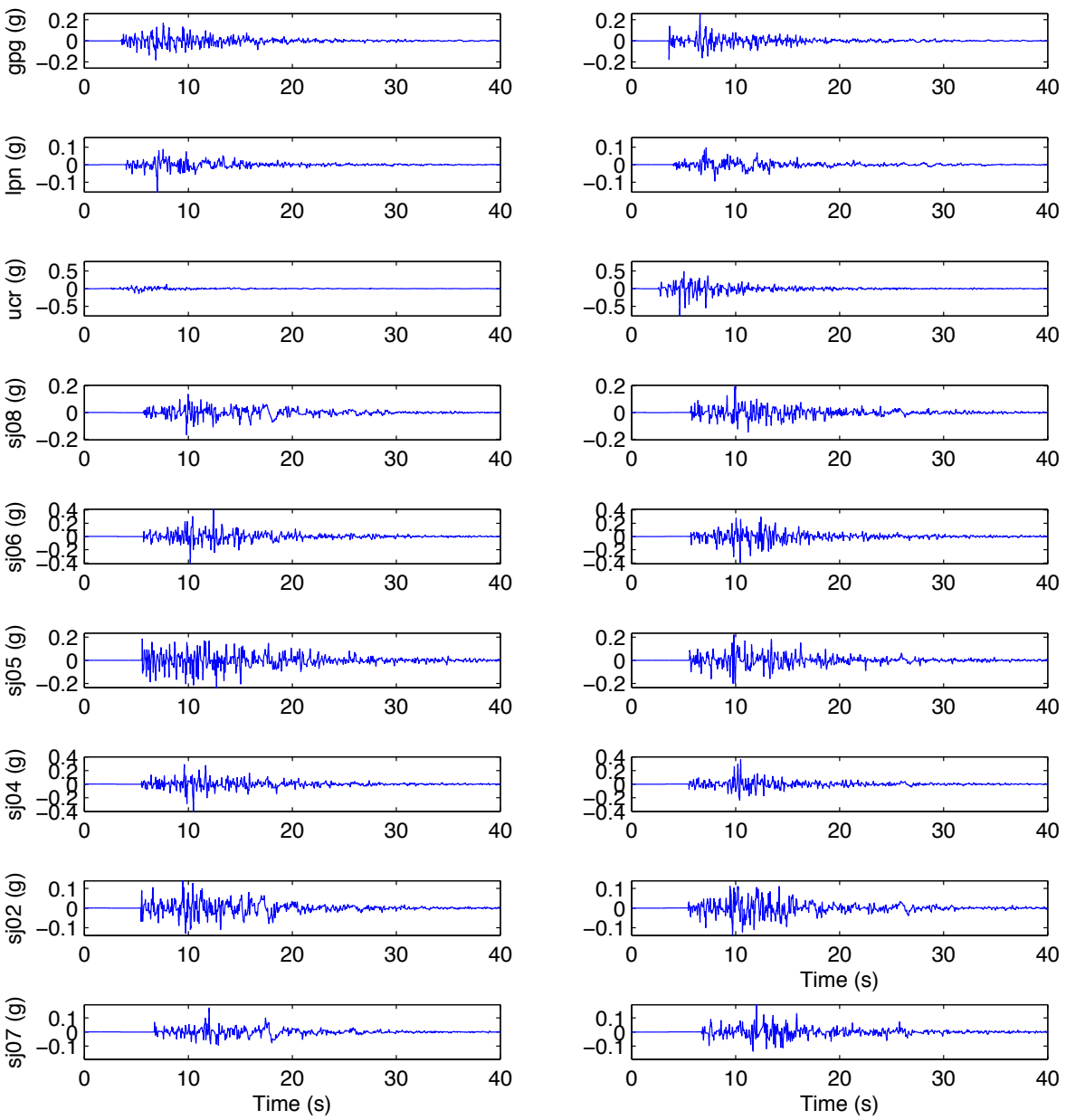

Figure B.1. Simulated horizontal accelerograms at the 20 PBR sites for rupture Scenario A1.

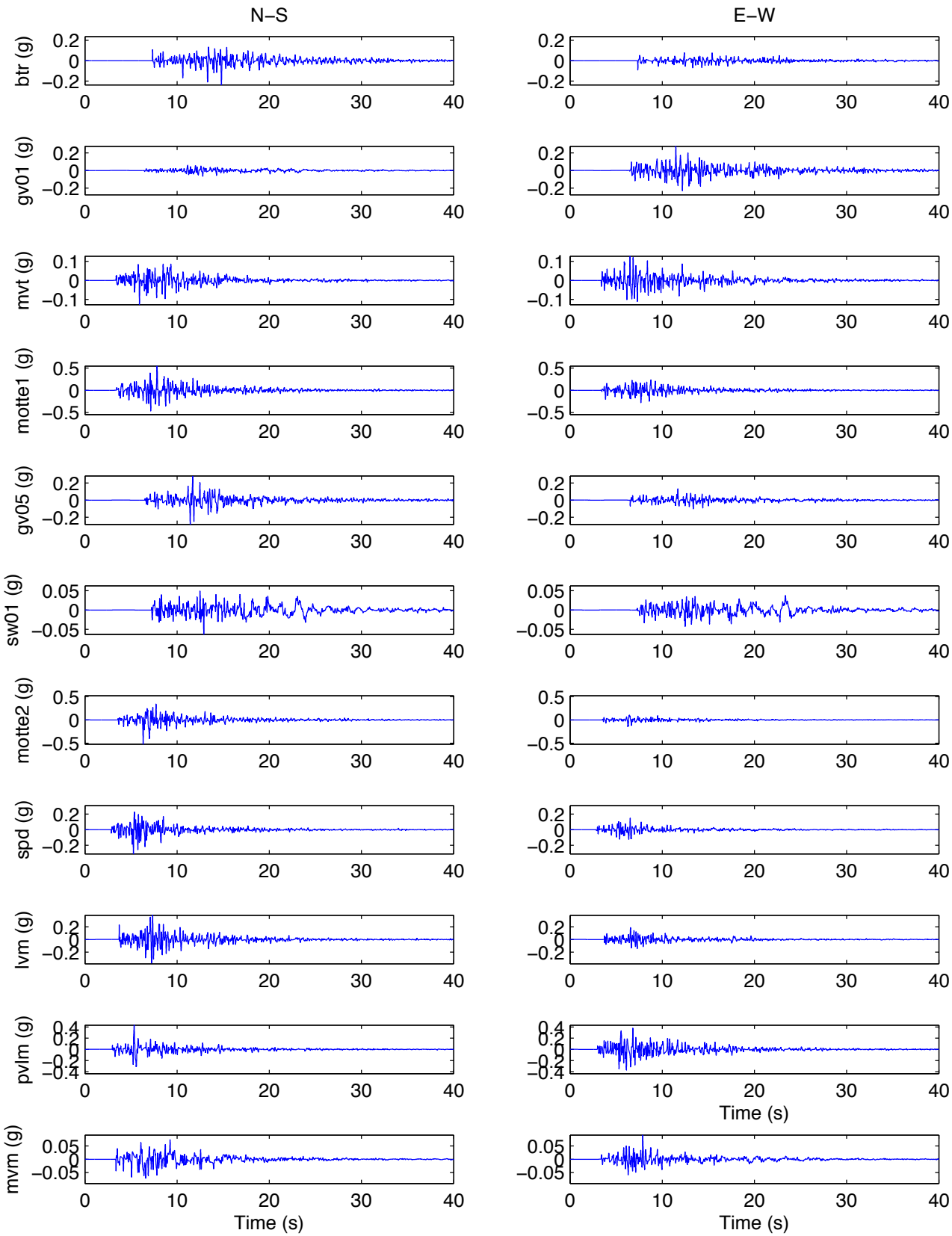
N−S
E−W
btr (g)
gv01 (g)
mvt (g)
motte1 (g)
gv05 (g)
sw01 (g)
motte2 (g)
spd (g)
lvm (g)
pvlm (g)
mvm (g)
Time (s)
Time (s)

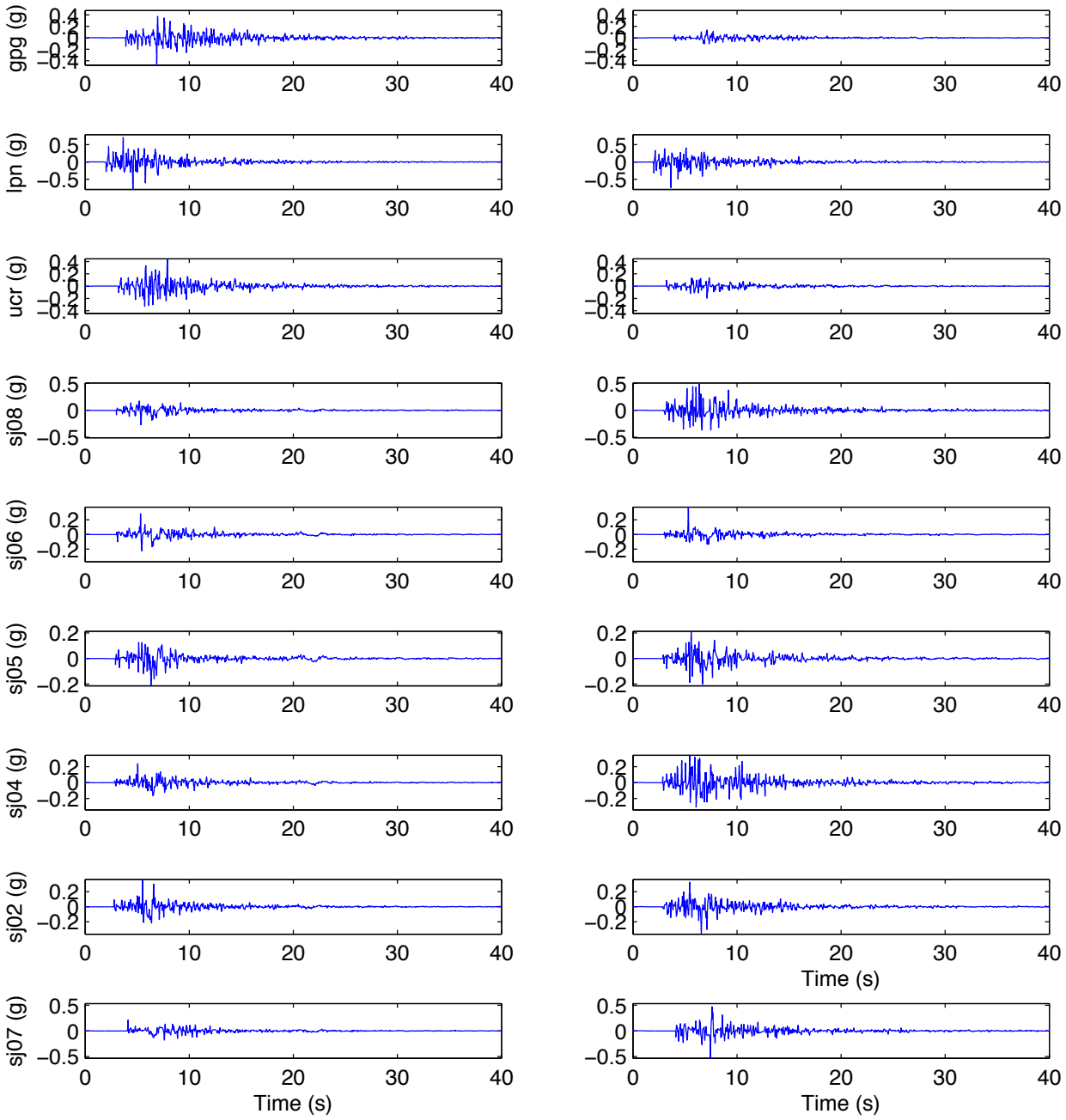

Figure B.2. Same as Fig. B.1, but for rupture scenario B2.

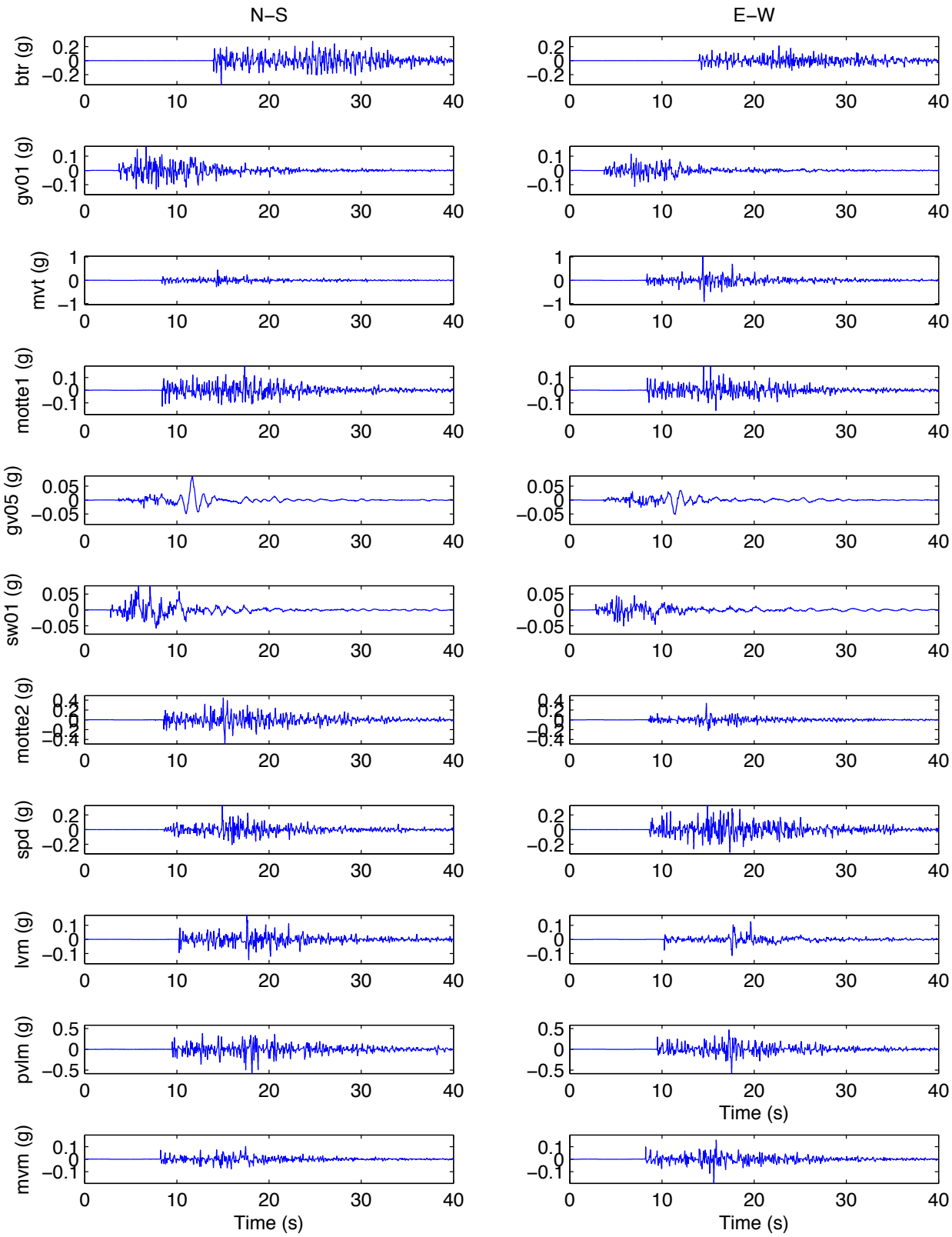
N–S
E–W
btr (g)
gv01 (g)
mvt (g)
motte1 (g)
gv05 (g)
sw01 (g)
motte2 (g)
spd (g)
lvm (g)
pvlm (g)
mvm (g)
Time (s)
Time (s)
Time (s)

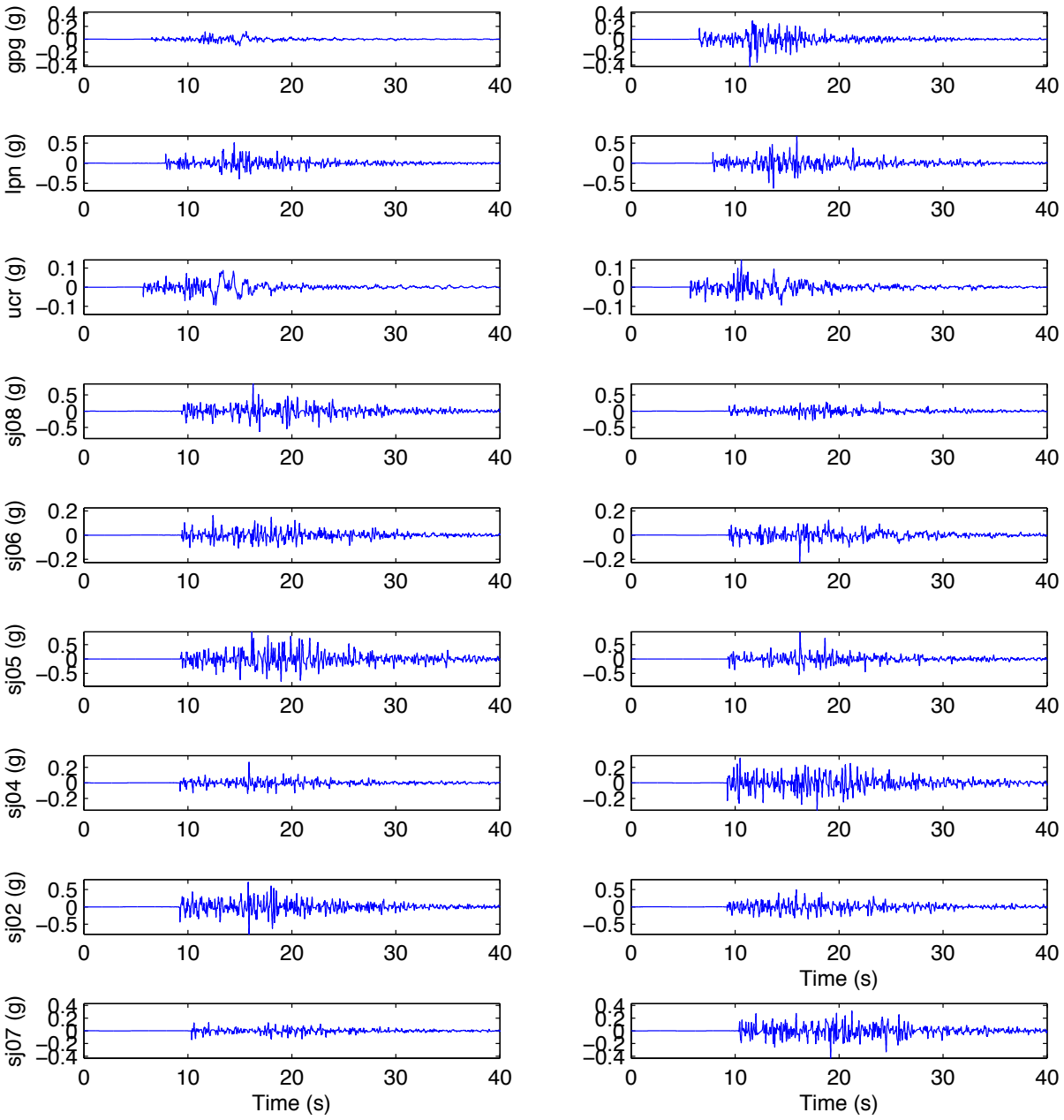

Figure B.3. Same as Fig. B.1, but for rupture scenario C1.

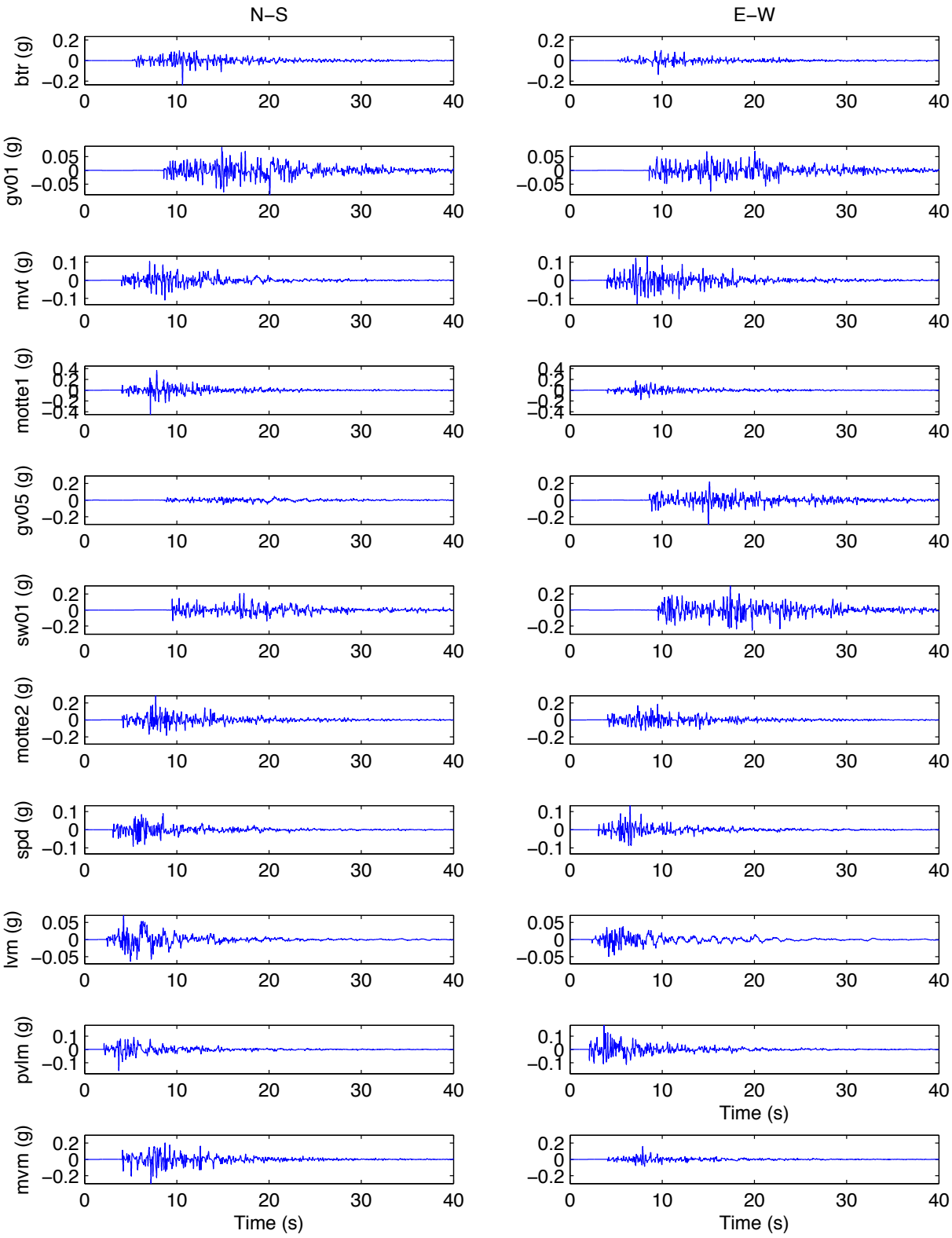
N−S
E−W
btr (g)
gv01 (g)
mvt (g)
motte1 (g)
gv05 (g)
sw01 (g)
motte2 (g)
spd (g)
lvm (g)
pvlm (g)
mvm (g)
Time (s)
Time (s)
Time (s)

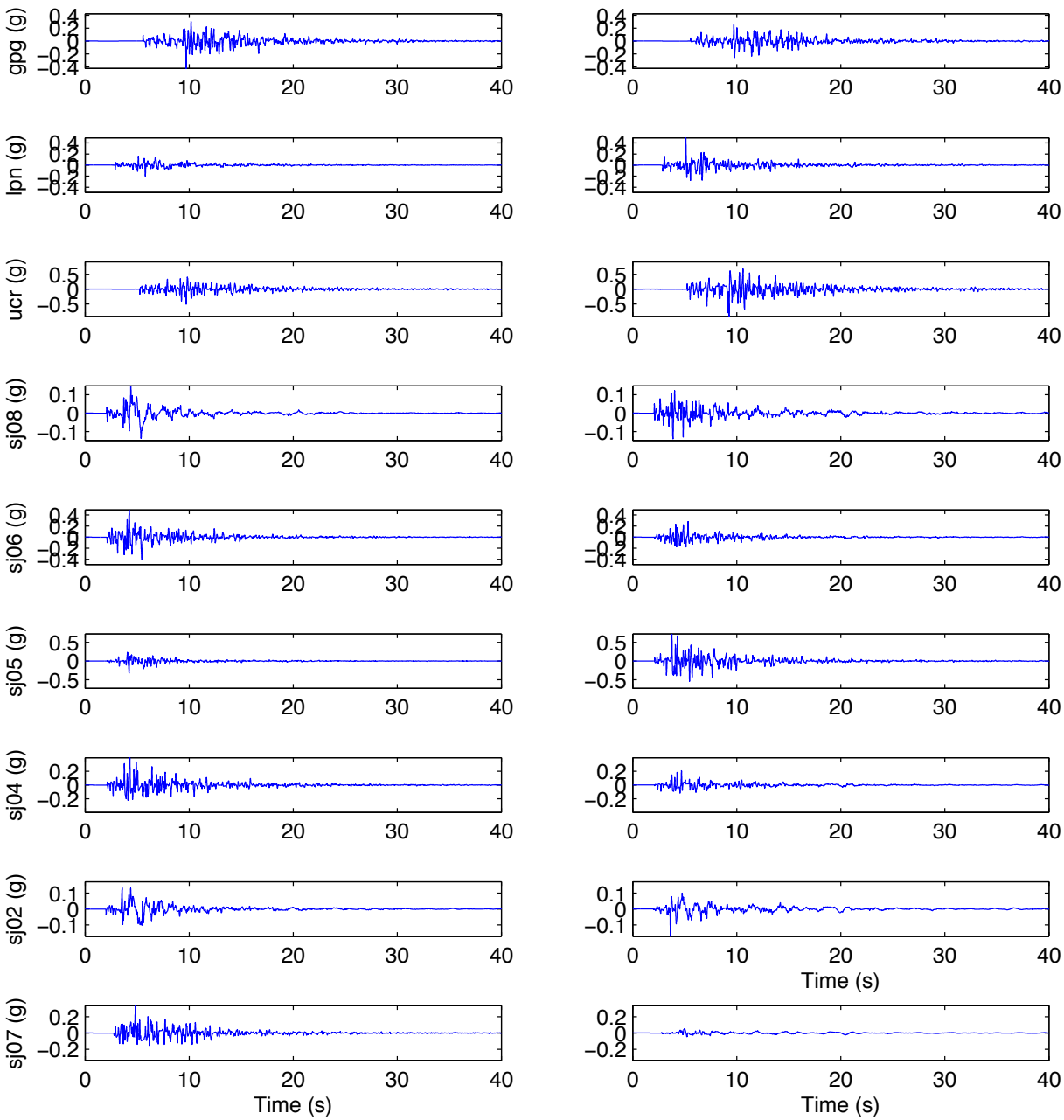

Figure B.4. Same as Fig. B.1, but for rupture scenario D2.

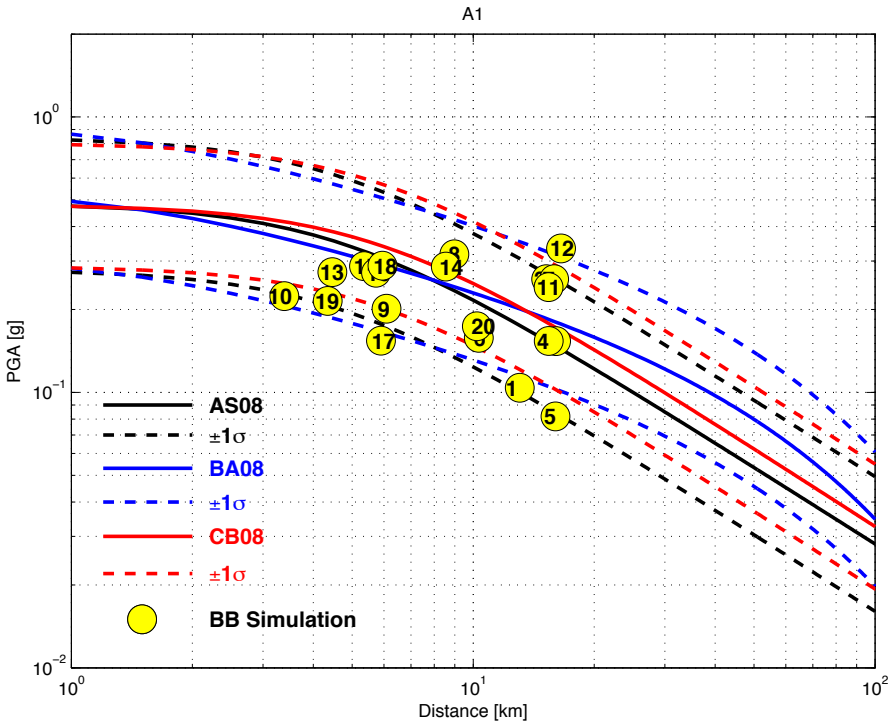
A1
PGA [g]
Distance [km]
AS08
±1σ
BA08
±1σ
CB08
±1σ
BB Simulation

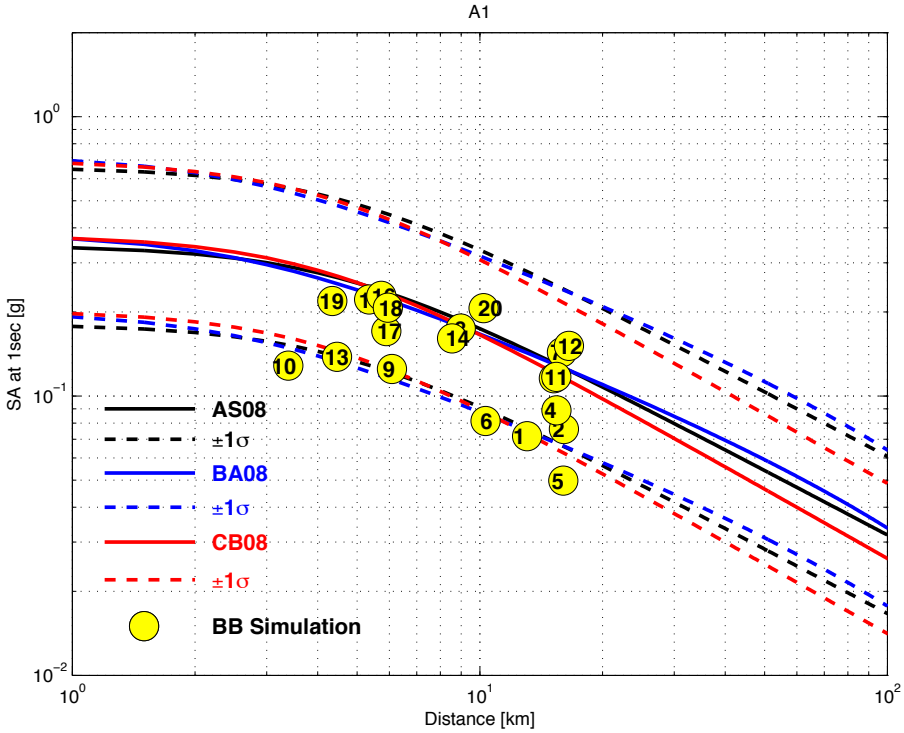
A1
SA at 1sec [g]
Distance [km]
AS08
±1σ
BA08
±1σ
CB08
±1σ
BB Simulation

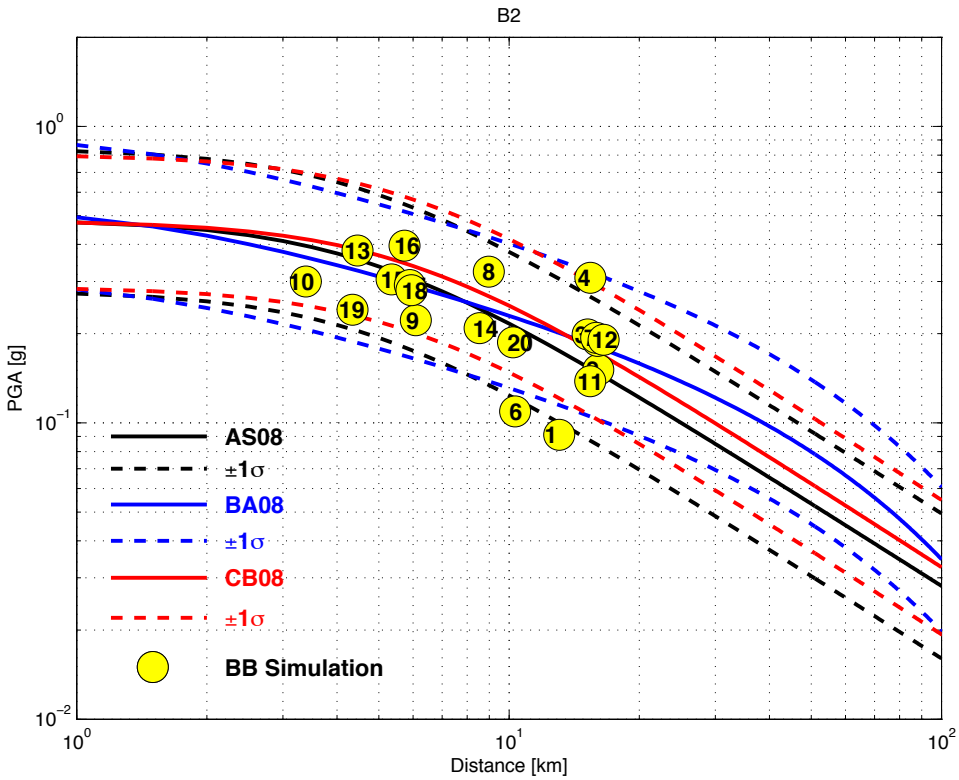
B2
PGA [g]
Distance [km]
AS08
±1σ
BA08
±1σ
CB08
±1σ
BB Simulation

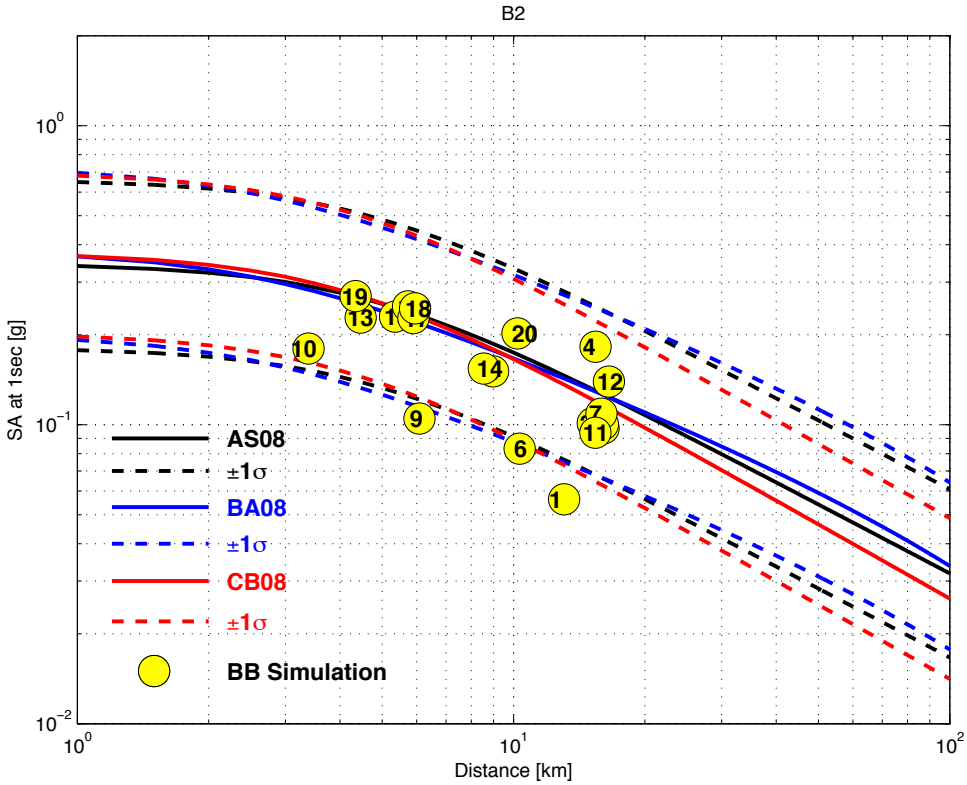
B2
SA at 1sec [g]
Distance [km]
AS08
±1σ
BA08
±1σ
CB08
±1σ
BB Simulation

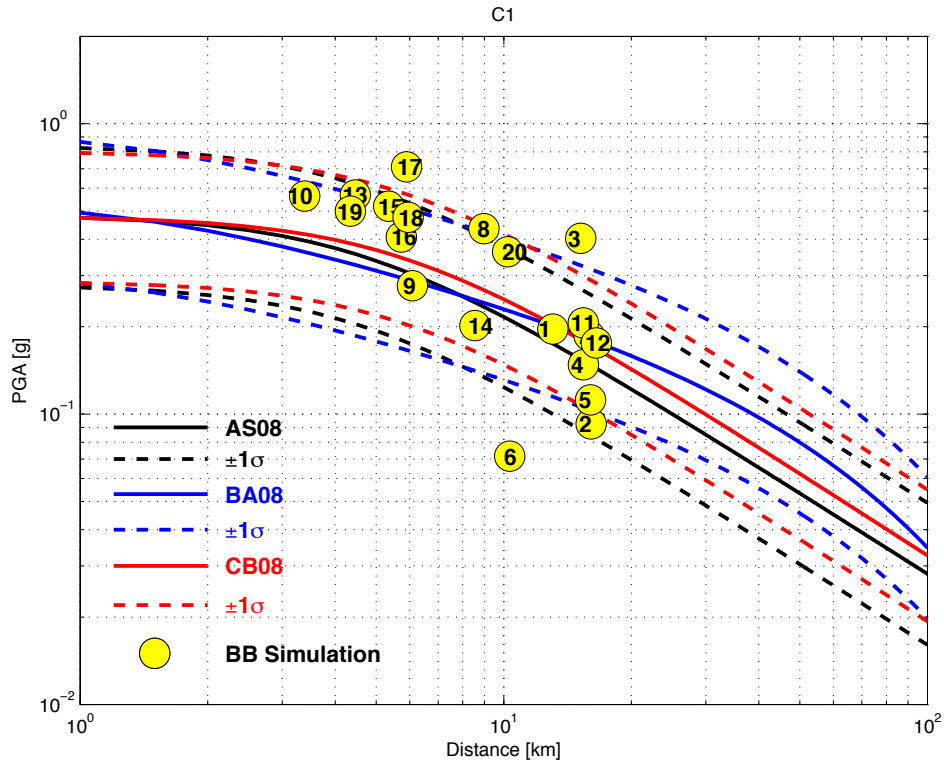
C1
PGA [g]
Distance [km]
AS08
±1σ
BA08
±1σ
CB08
±1σ
BB Simulation

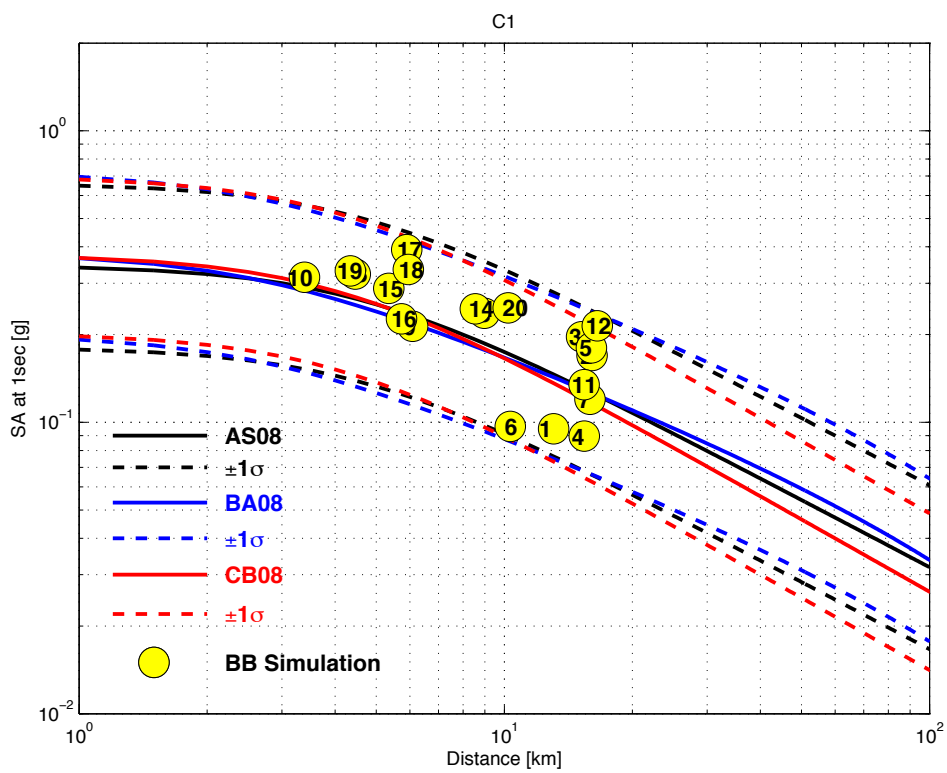
C1
SA at 1sec [g]
Distance [km]
AS08
±1σ
BA08
±1σ
CB08
±1σ
BB Simulation

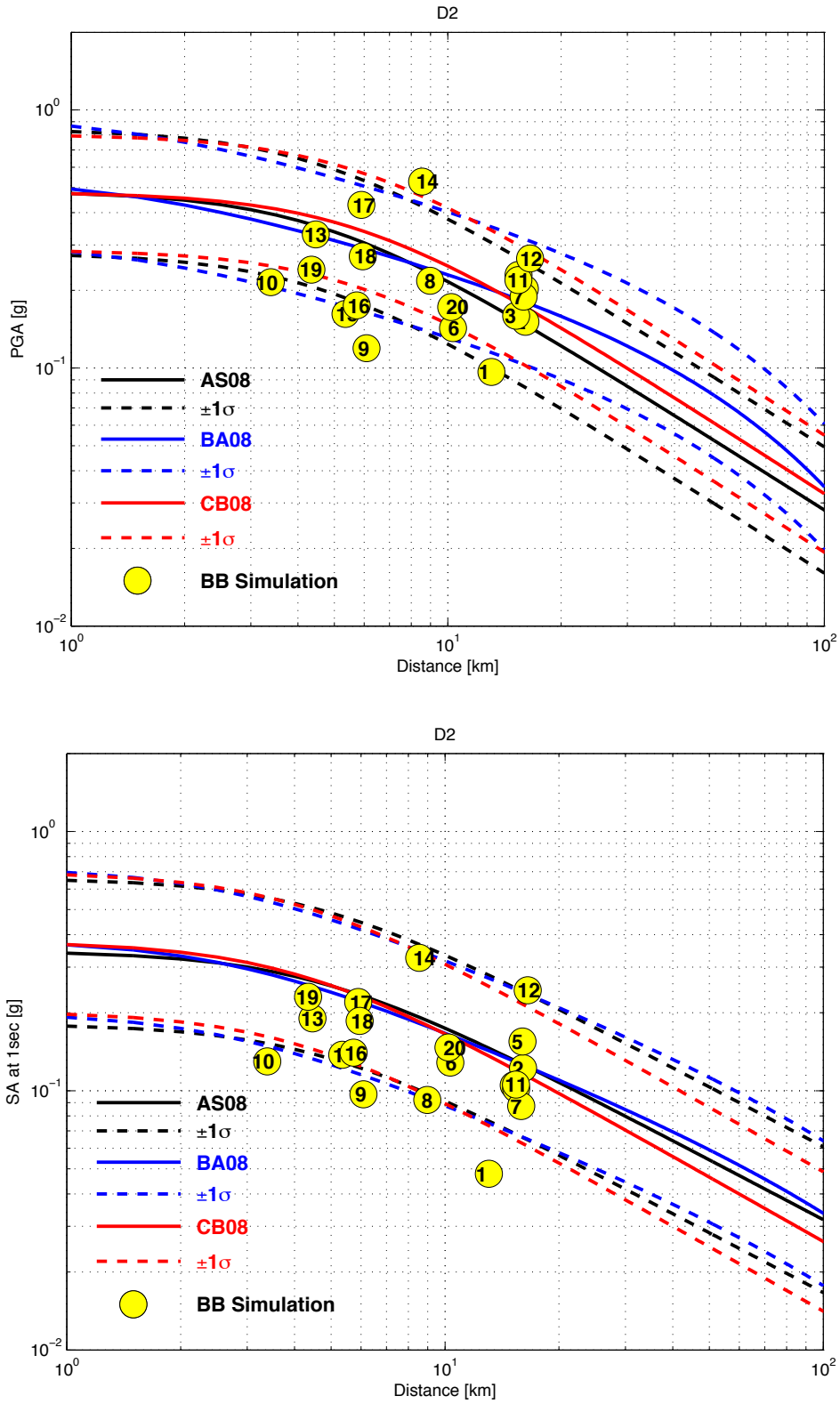

Figure B.5. Comparison of PGAs and SA-1s from the BBs to leading GMPEs.